Journal of Rock Mechanics and Geotechnical Engineering 14 (2022) 1609–1625

Contents lists available at ScienceDirect

Journal of Rock Mechanics and Geotechnical Engineering

journal homepage: www.jrmge.cn

Full Length Article

Real-time determination of sandy soil stiffness during vibratory compaction incorporating machine learning method for intelligent compaction

Zhengheng Xu, Hadi Khabbaz, Behzad Fatahi*, Di Wu

School of Civil and Environmental Engineering, University of Technology Sydney, Sydney, Australia

ARTICLE INFO

Article history:
Received 30 January 2022
Received in revised form
20 July 2022
Accepted 20 July 2022
Available online 4 August 2022

Keywords:
Intelligent compaction
Machine learning method
Finite element modelling
Acceleration response

ABSTRACT

An emerging real-time ground compaction and quality control, known as intelligent compaction (IC), has been applied for efficiently optimising the full-area compaction. Although IC technology can provide real-time assessment of uniformity of the compacted area, accurate determination of the soil stiffness required for quality control and design remains challenging. In this paper, a novel and advanced numerical model simulating the interaction of vibratory drum and soil beneath is developed. The model is capable of evaluating the nonlinear behaviour of underlying soil subjected to dynamic loading by capturing the variations of damping with the cyclic shear strains and degradation of soil modulus. The interaction of the drum and the soil is simulated via the finite element method to develop a comprehensive dataset capturing the dynamic responses of the drum and the soil. Indeed, more than a thousand three-dimensional (3D) numerical models covering various soil characteristics, roller weights, vibration amplitudes and frequencies were adopted. The developed dataset is then used to train the inverse solver using an innovative machine learning approach, i.e. the extended support vector regression, to simulate the stiffness of the compacted soil by adopting drum acceleration records. Furthermore, the impacts of the amplitude and frequency of the vibration on the level of underlying soil compaction are discussed. The proposed machine learning approach is promising for real-time extraction of actual soil stiffness during compaction. Results of the study can be employed by practising engineers to interpret roller drum acceleration data to estimate the level of compaction and ground stiffness during compaction.

1. Introduction

Implementing the stiffness-based soil compaction has recently gained an increasing interest during earthworks due to the popularity of the mechanistic pavement design procedures (Mooney, 2010; Mooney and Facas, 2013; Nazarian et al., 2020; Fathi et al., 2021a). The compacted soil must provide enough capacity to withstand the stresses from the top layers of the road, or the dynamic loads transmitted from the vehicles or trains and experience the minimal deformations (Ranasinghe et al., 2017; Scott et al., 2020; Hu et al., 2021). Consequently, non-destructive testing (NDT) as well as invasive testing, such as sand cone devices, are generally used to certify the satisfactory subgrade quality at discrete spots. Nevertheless, NDT spot testing methods cannot precisely assess the full-area compaction level and could leave the regions which are under-compacted or over-compacted undetected, potentially interfering with the project costs and impacting the road safety and the service life of the pavement. These issues can be overcome by properly implementing continuous compaction control (CCC) (Nazarian et al., 2020; Fathi et al., 2021a).

Fig. 1 shows a typical vibratory roller used for compaction of geomaterials, while the magnitude of the centrifugal force (F_{ecc}) can be automatically adjusted based on the contact force between the drum and soil (F_c). Adopting Newton's second law, the steady-state dynamic behaviour of the vibratory roller during vibration due to the centrifugal force applied to the drum via rotating eccentric mass can be written as below:

* Corresponding author.
E-mail address: behzad.fatahi@uts.edu.au (B. Fatahi).
Peer review under responsibility of Institute of Rock and Soil Mechanics, Chinese Academy of Sciences.

https://doi.org/10.1016/j.jrmge.2022.07.004

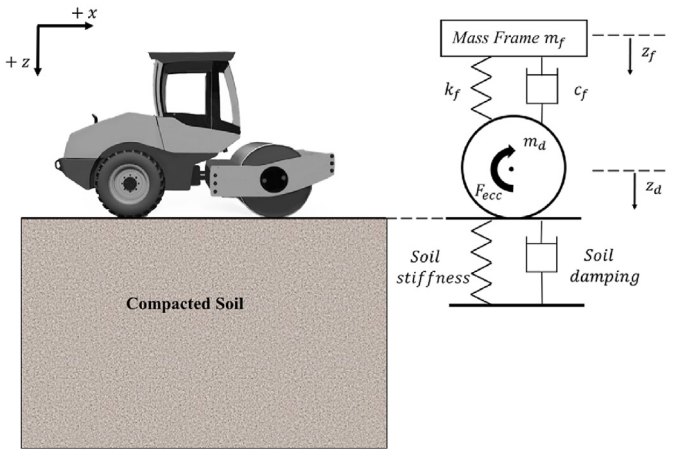

Fig. 1. Interaction behaviour between vibratory roller and compacted soil.

$$m_d\ddot{z}_d = F_{ecc} + m_d g + \left(\dot{z}_d - \dot{z}_f\right)c_f + \left(z_d - z_f\right)k_f - F_c \tag{1a}$$

$$m_f\ddot{z}_f = m_f g + \left(\dot{z}_f - \dot{z}_d\right)c_f + \left(z_f - z_d\right)k_f \tag{1b}$$

$$F_{ecc} = m_0 e_0 \omega^2 \cos(\omega t) \tag{2}$$

where F_c is the contact force; z_f, $\dot{z}_f$ and $\ddot{z}_f$ denote the displacement, velocity and acceleration of the vibratory roller frame, respectively; z_d, $\dot{z}_d$ and $\ddot{z}_d$ denote the displacement, velocity and acceleration of the vibratory roller drum, respectively; $m_0 e_0$ and ω are the eccentric mass moment and circular vibration frequency, respectively; m_d and m_f are the masses of the drum and frame, respectively; and k_f and c_f are the suspension modulus and suspension damping, respectively.

CCC technologies for vibratory rollers, which have been employed in the construction field for over 40 years, are associated with the dynamic analysis of the coupled roller-soil systems. Indeed, properties of the compacted layer during roller compaction can be detected by analysing the data collected from the accelerometer attached to the drum. Within CCC techniques, roller-integrated monitoring can measure underlying soil properties during compaction by incorporating the Global Positioning System and using response of the vibratory roller changing due to the soil stiffness to be used for real-time quality control during compaction and avoid early pavement deterioration (Xu et al., 2012; Asif Imran et al., 2018). Intelligent compaction (IC) technique is able to exhibit more uniform compaction and a more endurable performance (Xu et al., 2012). Hence, it is of prime importance to allow practising engineers to thoroughly understand mechanism of the interaction between the drum and the underlying soil (Bhandari et al., 2022; Xu et al., 2022). IC measurement values (ICMVs) are generic terms determined based on roller acceleration response during compaction, which could be applied to evaluating the uniformity of the compacted region and correlating to geomaterial for its physical and mechanical characteristics. Indeed, historically, a dimensionless parameter, known as compaction meter value (CMV), incorporating the harmonic signal of the drum and its acceleration amplitude, can be correlated to stiffness of underlying geomaterial and soil compaction level (Forssblad, 1980). Furthermore, by measuring the sub-harmonic content of the roller acceleration and temperature, compaction control value, an extension of CMV, could be utilised to assess the compaction level of the asphalt (Chang et al., 2011; Xu et al., 2012). More recently, an increasing emphasis has been given to the investigation of the composite nature of soil stiffness (k_s) considering drum loading conditions and roller responses, and generally based on the assumption of the rigid cylinder vibrating on the elastic half-space (Lundberg, 1939; Krober et al., 2001; Anderegg and Kaufmann, 2004; Van Susante and Mooney, 2008; Kenneally et al., 2015).

US Department of Transportation (US DOTs) (FHWA, 2017) identified five levels and precisions for roller data interpretation, i.e. (i) empirical models based on frequency response, (ii) empirical energy models with rolling resistance, (iii) simplified static mechanistic models, (iv) dynamic mechanistic models and (v) dynamic models with artificial intelligence (Table 1). The empirical solutions according to the frequency responses and rolling resistance are the most basic ICMVs, which require specific machine parameters such as energy loss and machine movement angle. The use of these empirical approaches is computationally time-consuming and very sensitive to machine parameters, which are complex to determine. In more recent studies (Beainy et al., 2014; Adam and Pistrol, 2016), the dynamic roller behaviour is employed to assess the compaction quality according to the roller vibration displacement, velocity and acceleration.

The physical models capturing the roller characteristics and the properties of compacted geomaterial were also utilised to estimate the interaction between drum and soil (Anderegg and Kaufmann, 2004; Mooney and Rinehart, 2007; Van Susante and Mooney, 2008; Pei and Yang, 2018). The majority of experimental studies were conducted to better understand and assess the influences of drum characteristics on the achieved soil stiffness during the compaction process (Mooney and Rinehart, 2009). Van Susante and Mooney (2008) applied the simplified numerical model based on the added mass technique for soil modelling to evaluate the roller integrated experimental data to reflect the interaction between the soil and the drum. However, due to the excessively simplified assumptions for dissipative and inertial properties in this technique, a site-specific calibration would be necessary (Kenneally et al., 2015). Additionally, Buechler et al. (2012) demonstrated that the discrete element method (DEM) is capable of simulating the soil-structure interaction and evaluating the mechanical responses as well as macroscopic deformations based on microstructural interactions. However, the very long computational time for DEM does not yet allow this technique to be used for the real-time assessment of compaction levels (Beainy et al., 2014; Fathi, 2020). Although Mooney and Facas (2013) attempted to optimise the modelling features and size using boundary element modelling (BEM), those models still cannot explicitly portray the soil-drum system accurately and need iterative processes and indirect means to capture the soil response (Mooney and Facas, 2013; Fathi, 2020).

Table 1
Five levels and precisions for roller data interpretation (modified after FHWA, 2017).

Level	Description	Measurement value	Correlation	Model type
1	Empirical models based on frequency response	Harmonic ratio	Poor or week	N/A
2	Empirical energy models with rolling resistance	Energy index	Poor or weak	Dynamic/ static
3	Simplified static mechanistic models	Stiffness, modulus, resistance force	Satisfactory	Dynamic
4	Dynamic models	Modulus, resistance force	Good	Dynamic
5	Dynamic models with artificial intelligence	Modulus, density	Excellent	Dynamic

Several researchers used the finite element method (FEM), adopting a continuum-based computational technique to explain the interaction mechanism between drum and soil (Xu et al., 2012; Erdmann and Adam, 2014; Kenneally et al., 2015; Herrera et al., 2018; Fathi, 2020; Nazarian et al., 2020). Kenneally et al. (2015) used a two-dimensional (2D) FEM adopting a linear elastic constitutive soil model for a uniform soil profile to explore the impacts of the compacted layer modulus and thickness on the dynamic response of the roller. Since the simplified 2D model assumes a uniform load distribution along the drum length, three-dimensional (3D) models capturing a more realistic distribution of load below the roller are certainly more accurate and preferable. For example, Fathi (2020) adopted a 3D finite model to evaluate responses of the compacted soil layer during roller proof-mapping. It should be noted that the majority of studies simulating the interaction between the roller and drum explicitly considered the linear elastic (Van Susante and Mooney, 2008; Mooney and Facas, 2013) or viscoelastic soil models (Erdmann and Adam, 2014; Herrera et al., 2018). Indeed, many previous studies have shown that considering soil nonlinearity subjected to cyclic loading is paramount when soil deformation or reaction forces need to be predicted, and thus suitable constitutive models often with many model parameters need to be adopted in the modelling (Liu et al., 2014; Saberi et al., 2020). However, practising engineers need constitutive models with fewer parameters that can be obtained from common geotechnical tests or from the existing correlations to other soil parameters (Brinkgreve et al., 2010; Alzabeebee, 2021). For example, the addition of the Rayleigh damping feature to linear elastic models can somehow compensate for the missing hysteresis damping, while stiffness degradation and dependency of parameters to stress level and number of loading cycles need more rigorous constitutive models (Kontoe et al., 2011; Alzabeebee, 2021). In general, a reasonable soil constitutive model needs to capture variations of soil damping and stiffness with the cyclic shear strain and cumulative plastic deformations during cyclic loading.

With the increasing demand for earthworks, particularly for infrastructure projects advancement of IC, the solutions for the dynamic behaviour of interacting systems have been utilised as the prominent basis of more recent modellings. Fathi et al. (2021a) integrated the data from the 3D numerical modelling and field to assess the depth of influence of IC rollers. They exhibited an interrelationship between the soil type and the influence depth. Results illustrated that as geomaterial became more granular, the depth of influence would increase, while the influence would decrease as the soil became more cohesive. In addition, IC technology by integrating dynamic mechanical solutions with artificial intelligence has recently been carried out to increase the compaction quality. Cao et al. (2021) adopted an artificial neural network (ANN) to predict CMV based on the roller-related factors, which is consistent with the collected test data. An et al. (2020) proposed an approach to optimise the compaction process using a genetic algorithm (GA) to decide the number of passes. These solutions demonstrate the possibility of using new techniques to efficiently enhance the accuracy of IC results.

In this study, a hardening soil with small-strain stiffness (HS-Small) constitutive model was employed to simulate the various soil properties and investigate the interaction of the vibratory drum and the soil beneath. The key motivation for this study is to establish a rigorous and efficient method that can rapidly and accurately extract the compacted soil stiffness according to the vibratory response of the drum. Therefore, results of more than a thousand 3D numerical models were adopted to develop a dataset covering loose to dense sandy soils, roller weights, vibration amplitudes and frequencies. The developed dataset was then used to train the inverse solver using extended support vector regression (X-SVR) with the Gegenbauer kernel function to estimate the stiffness of the compacted soil adopting drum acceleration records.

2. Development of 3D numerical model

2.1. Overview of the model

The dynamic response of the vibratory roller on the compacted underlying soil was evaluated using the finite element program PLAXIS 3D in this study (Brinkgreve et al., 2016). The 3D FEM was carried out to predict the influences of interaction between the drum and the soil beneath and the way in which the soil characteristics impacted the drum response. A typical vibrating rigid, smooth drum sitting on a uniform soil deposit was modelled using the continuum-based approach with appropriate material properties and geometries assigned to each component. Fig. 2a exhibits the 3D view of the cylindrical rigid drum roller resting on the soil layer. The adopted roller drum was 1.5 m in diameter and 2.1 m in length, corresponding to typical drum sizes used in Australia for earthworks in major infrastructure projects. The weight of the roller was considered as a variable changing between 6 t and 20 t.

Loading conditions for a given vibratory roller are defined by the frequency and amplitude of the loading, which depends on the frequency of its rotation, eccentricity and eccentric mass, and can impact the productivity of the roller significantly (Lavin, 2003). Therefore, to simulate the behaviour of a vibrating drum, an eccentric mass m_0 rotating around the axle of the drum with an effective moment arm e_0 was considered to induce the centrifugal force corresponding to the eccentric mass moment m_0e_0 varying between 1 kg m and 9 kg m (Fig. 2b). In addition, the applied excitation frequency ranged from 20 Hz to 35 Hz, which together with different eccentric mass moments, could result in a wide practical range of centrifugal forces (F_{ecc}) as in Eq. (2).

In this study, the vibration force as in Eq. (2) was applied to the drum via distributed line load to simulate the vibratory behaviour induced by the rotating eccentric mass. Table 2 summarises the adopted roller specifications and the variation ranges used in this study for parametric study.

The soil compaction via vibratory roller is induced by the combination of static forces (weights of frame and drum) as well as dynamic forces (the counter-rotating eccentric masses resulted in centrifugal force). The multi-degree of freedom roller (MDOF) vibration system with various components, including the drum, frame, back tire and cabin, can represent the entire system more accurately. However, for the sake of simplicity and practicality, the single degree of freedom system for the drum is often implemented which can capture the most significant impact force induced by the vibrating drum (Herrera et al., 2018; Bhandari et al., 2022; Xu et al., 2022). Additionally, low stiffness rubbers separate the compactor frame from the drum, leading to the effects of the dynamic frame being insignificant, resulting in frame dynamic effects often being neglected in the analysis (Kenneally et al., 2015; Herrera et al., 2018; Nazarian et al., 2020; Xu et al., 2022).

2.2. Modelling of soil

Consideration of soil nonlinearity when simulating soil-structure interaction is of critical importance (Brinkgreve et al., 2010; Han et al., 2016). Indeed, simple elastic or viscoelastic constitutive models are unable to simulate the soil deformation and forces transferred from the soil to the roller accurately, impacting its acceleration response (Herrera et al., 2018; Zhang and Kimura, 2002; Fatahi et al., 2020). Thus, it is crucial to adopt a suitable constitutive model for capturing the nonlinear stress-strain response of the underlying soil properties subjected to cyclic

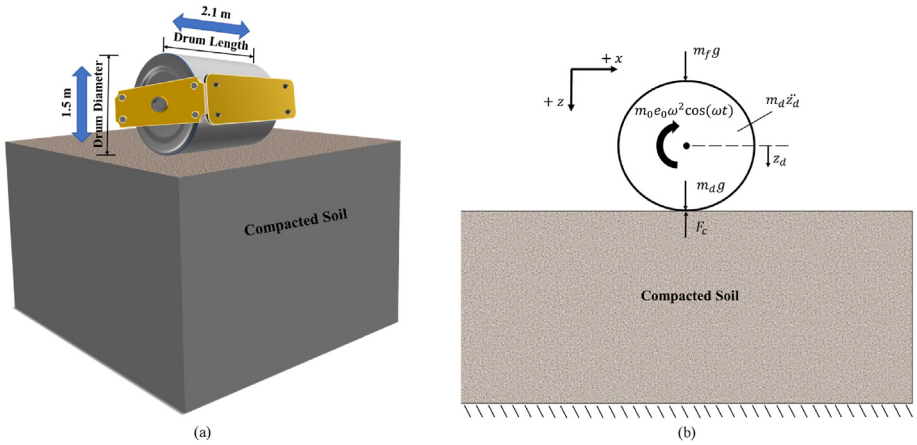

Fig. 2. Vibratory roller compactor system: (a) Sketch of the drum and (b) Free body diagram of one degree of freedom lumped mass model for vertical forces acting on compacted soil.

Table 2
Operational values of vibratory roller adopted in this study.

Parameter	Unit	Minimum	Maximum
Radius of drum	m	0.75	0.75
Length of drum	m	2.1	2.1
Mass of roller	kg	5000	20,000
Eccentric mass moment	kg m	1	9
Vibration excitation frequency	Hz	15	35

loading, specifically by capturing damping with shear strain and variations of soil stiffness and allowing the prediction of permanent soil deformations during compaction (Brinkgreve et al., 2010; Sharma and Kumar, 2018; Nazarian et al., 2020). In this study, the soil response subjected to cyclic loading was evaluated by applying the HS-Small model developed by Benz (2007). This model could capture stiffness degradation as well as the stress-strain dependant stiffness in the small and large strain ranges. The small-strain stiffness is a fundamental characteristic of geomaterials, including rocks, gravels, sands, silts and clays under different loading conditions (Burland, 1989; Kuwano, 2018). According to Benz et al. (2009), the HS-Small model is able to simulate the modulus decay and hysteretic damping of the soils at the small strain range. The model is suitable for modelling different soil types since the vast of the model input parameters can simply be simulated on the basis of triaxial drained test results, which can also be verified using the cone penetration (CPT) field tests and seismic dilatometer (SDMT) results (Kawa et al., 2021). Therefore, the model has gained popularity for its application in geotechnical practice as all input parameters have a clear geotechnical relevance (Schanz et al., 2019; Kawa et al., 2021). In this study, the HS-Small model was applied for simulating the cyclic behaviour of sandy soils from small to large strains, and the pressure dependency of the modulus, which is critical for sandy soils, was captured.

HS-Small model needs six stiffness related parameters defined at a reference pressure of p^{ref} (= 100 kPa in this study), i.e. E_{50}^{ref} and $E_{\mathrm{oed}}^{\mathrm{ref}}$, which are the secant and tangent stiffnesses, respectively; $E_{\mathrm{ur}}^{\mathrm{ref}}$ representing the unloading/reloading stiffness; and ν_{ur} indicating the Poisson's ratio for unloading/reloading cycles. The small-strain shear stiffness (G_0) and a shear strain ($\gamma_{0.7}$) are used to describe the shape of the G_s-γ_c relationship. Additionally, three measurable strength parameters were used for adopting the Mohr-Coulomb failure criterion, known as c_{ref} (cohesion), ψ (angle of dilatancy) and φ (angle of friction). Moreover, two empirical inputs, i.e. failure ratio (R_f) and power for the stress-level dependency of stiffness (m) are required in the model as explained below.

According to Brinkgreve et al. (2016), these key stiffness inputs required in this model are: (i) the one-dimensional (1D) tangent stiffness modulus (E_{oed}), (ii) the stress-dependent stiffness modulus for highly nonlinear primary deviatoric loading (E_{50}), and (iii) the unloading and reloading stress-dependent stiffness (E_{ur}), as captured in Eqs. (3)–(5), respectively:

$$E_{\mathrm{oed}} = E_{\mathrm{oed}}^{\mathrm{ref}} \left(\frac{c\cos\varphi - \frac{\sigma_3 \sin\varphi}{K_0^{\mathrm{nc}}}}{p^{\mathrm{ref}}\sin\varphi + c\cos\varphi} \right)^m \tag{3}$$

$$E_{50} = E_{50}^{\mathrm{ref}} \left(\frac{c\cos\varphi - \sigma_3 \sin\varphi}{p^{\mathrm{ref}}\sin\varphi + c\cos\varphi} \right)^m \tag{4}$$

$$E_{\mathrm{ur}} = E_{\mathrm{ur}}^{\mathrm{ref}} \left(\frac{c\cos\varphi - \sigma_3 \sin\varphi}{p^{\mathrm{ref}}\sin\varphi + c\cos\varphi} \right)^m \tag{5}$$

where K_0^{nc} denotes the stress ratio, and σ_3 is the minor principal stress. Furthermore, the hyperbolic function between the vertical strain, ε_1, and the deviatoric stress, q, is the fundamental concept for the formulation of the HS-Small model and can be given by the below equation:

$$-\varepsilon_1 = \frac{2 - R_f}{2E_{50}} \frac{q}{1 - \frac{q}{q_a}} \tag{6}$$

where q_a is the asymptotic value of the shear strength. Additionally, the HS-Small model is specifically designed to simulate the soil plasticity and hysteretic damping of soil at large and small strains, respectively, while considering isotropic hardening (Brinkgreve et al., 2007; Schanz et al., 2019). The model incorporates the modified Hardin and Drnevich (1972) model as proposed by Dos Santos and Correia (2001) for strain-dependent stiffness, as in Eqs. (7) and (8):

$$G_s = \frac{G_0}{1 + \frac{\alpha\gamma_c}{\gamma_{0.7}}} \tag{7}$$

$$G_0 = G_0^{\mathrm{ref}} \left(\frac{c\cos\varphi - \sigma_3 \sin\varphi}{p^{\mathrm{ref}} \sin\varphi + c\cos\varphi} \right)^m \tag{8}$$

where G_0 and G_s are small-strain and secant shear stiffnesses, receptively; γ_c is the shear strain; $\gamma_{0.7}$ represents the shear strain at which $G_s/G_0 = 0.7$; and G_0^{ref} is the shear modulus at the reference pressure p^{ref}. It is advised to set the model parameter α (the constant in Eq. (7)) to 0.385 in order to reach a satisfactory agreement with laboratory measurements. The small strain tangent shear modulus (G_t) is calculated from Eq. (9), capturing the stiffness degradation at the small strain range.

$$G_t = \frac{G_0}{\left(1 + \frac{\alpha\gamma_c}{\gamma_{0.7}}\right)^2} \geq G_{ur} \tag{9}$$

where G_{ur} is the unloading/reloading shear modulus. Additionally, the model implicitly captures the soil hysteretic damping via stiffness degradation with the governing equations as follows:

$$\xi = \frac{E_D}{4\pi E_S} \tag{10}$$

$$E_D = \frac{4G_0\gamma_{0.7}}{\alpha} \left[2\gamma_c - \frac{\gamma_c}{1 + \frac{\gamma_{0.7}}{\alpha\gamma_c}} - \frac{2\gamma_{0.7}}{\alpha} \ln\left(1 + \frac{\alpha\gamma_c}{\gamma_{0.7}}\right) \right] \tag{11}$$

$$E_S = \frac{1}{2} G_S \gamma_c^2 = \frac{G_0 \gamma_c^2}{2 + \frac{2\alpha\gamma_c}{\gamma_{0.7}}} \tag{12}$$

where ξ is the hysteretic damping ratio; and E_D and E_S are the dissipated energy and the cyclic maximum strain energy in a single loading cycle, respectively.

The key motivation for this study is to develop an advanced tool that can rapidly and reasonably extract the compacted soil stiffness for sandy soil based on the vibration responses of the drum during compaction. Thus, in order to investigate the drum responses under various soil properties, different states of sandy soil ranging from relative density $RD = 20\%$–90% were considered to address the soil properties from loose to dense from early stages of compaction to a well-compacted condition. Table 3 summarises the adopted soil characteristics corresponding to different relative densities for the HS-Small model following the formulations proposed by Brinkgreve et al. (2010). Fig. 3a and b exhibits the damping ratio and stiffness degradation curves adopted in the paper, respectively. In addition, the water table was considered to be deep, leading to no significant excess pore water pressure being generated during the compaction process (Fatahi et al., 2020).

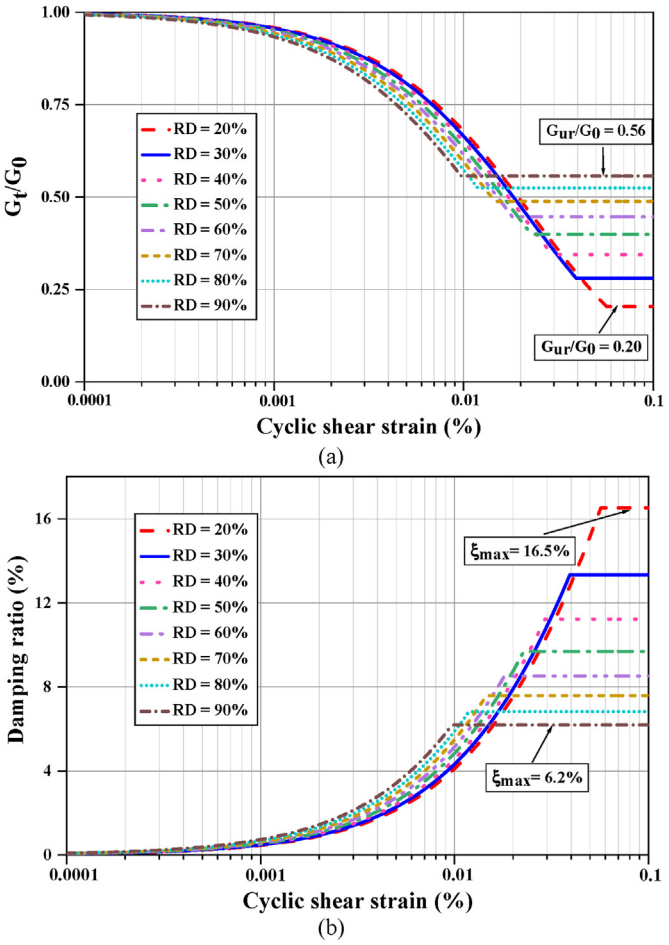

Fig. 3. (a) Tangent shear modulus degradation curve for different relative densities and (b) Damping ratio curves for different relative densities.

To validate the reliability of the FEM prediction and assess the suitability of the adopted soil constitutive model, the developed numerical simulations with the HS-Small model results were compared with the data reported by Wu (1990) for triaxial tests conducted on Karlsruhe sand for different relative densities at 100 kN/m^2 cell pressure, as shown in Fig. 4. It has been shown that

Table 3
Adopted soil parameter for hardening soil model with small-strain stiffness for different relative densities.

Parameter	Value							
	$RD = 20\%$	$RD = 30\%$	$RD = 40\%$	$RD = 50\%$	$RD = 60\%$	$RD = 70\%$	$RD = 80\%$	$RD = 90\%$
p^{ref} (kPa)	100	100	100	100	100	100	100	100
γ(kN/m^3)	15.8	16.2	16.6	17	17.4	17.8	18.2	18.6
E_{50}^{ref} (kPa)	12,000	18,000	24,000	30,000	36,000	42,000	48,000	54,000
E_{oed}^{ref} (kPa)	12,000	18,000	24,000	30,000	36,000	42,000	48,000	54,000
E_{ur}^{ref} (kPa)	36,000	54,000	72,000	90,000	108,000	126,000	144,000	162,000
G_0^{ref} (kPa)	73,600	80,400	87,200	94,000	100,800	107,600	114,400	121,200
M	0.6375	0.6063	0.575	0.5438	0.5125	0.4813	0.45	0.4188
$\gamma_{0.7}$	1.8×10^{-4}	1.7×10^{-4}	1.6×10^{-4}	1.5×10^{-4}	1.4×10^{-4}	1.3×10^{-4}	1.2×10^{-4}	1.1×10^{-4}
φ (°)	30.5	31.75	33	34.25	35.5	36.75	38	39.25
ψ (°)	0.5	1.75	3	4.25	5.5	6.75	8	9.25
R_f	0.975	0.963	0.95	0.938	0.925	0.913	0.9	0.888
ϑ_{ur}	0.2	0.2	0.2	0.2	0.2	0.2	0.2	0.2

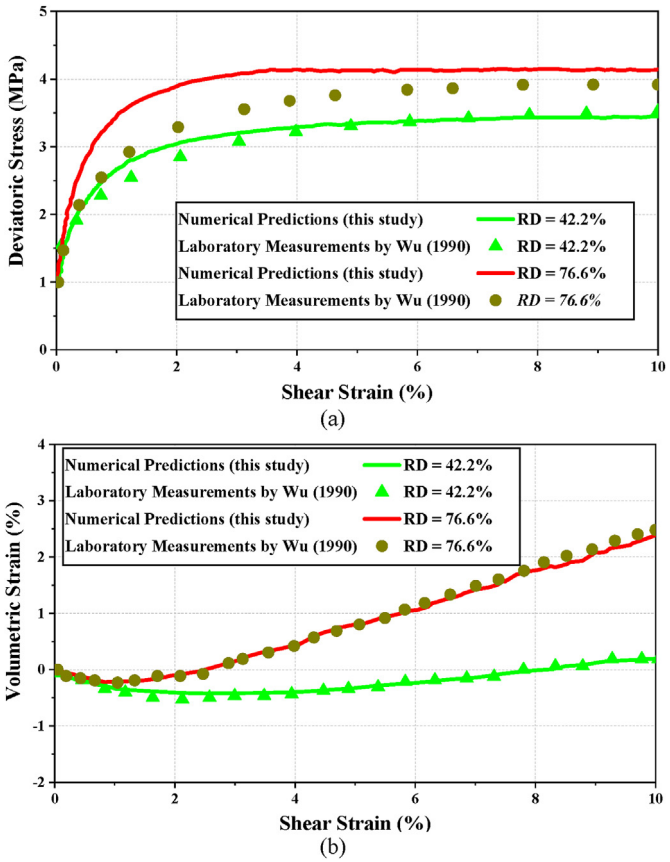

Fig. 4. Comparison between the drained triaxial test results on Karlsruhe sand and HS-Small model predictions and those obtained based on proposed correlations for different relative densities by Wu (1990): (a) Deviatoric stress vs. shear strain for different relative densities, and (b) Volumetric strain vs. shear strain for different relative densities.

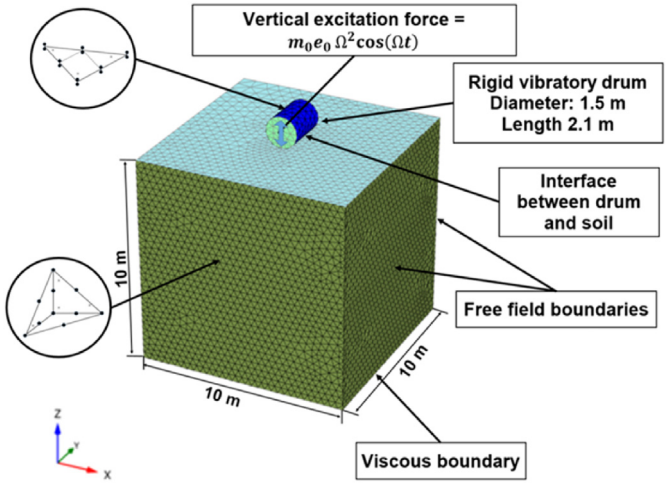

Fig. 5. Adopted 3D numerical model capturing the interaction between drum and soil.

the predicted results, which accept correlations for the model parameters as provided by Brinkgreve et al. (2010), are in a respectable agreement with the experimental data. The model can reasonably predict the deviatoric stresses and volumetric strains of both loose and dense sandy soils.

2.3. Geometrical characteristics of the model

Referring to Fig. 5, to characterise the interaction between the drum and underlying soil, a 3D numerical model of a vibrating drum on a soil deposit was established to predict the time history of the roller acceleration response during vibration. To simulate the weight of the roller, gravity load was employed on the rigid drum. Moreover, the vibratory loading of the drum was achieved by applying the eccentric force as in Eq. (2). It should be noted that no horizontal forces were applied to the roller, assuming that the eccentric mass configuration inside the drum, which rotates along the longitudinal axis of the drum, nullified the horizontal forces (Van Susante and Mooney, 2008).

For the sake of accuracy and minimising the boundary effects, a block of soil that was 10 m in length, 10 m in depth, and 10 m in width was modelled by applying the 10-node tetrahedral elements (Fig. 5). Each node in the underlying soil had three degrees of freedom which allowed a second-order interpolation for displacement, making the arrangement suitable for dynamic analysis. In addition, the influence depth of the adopted vibratory roller was simulated to be 0.6–1 m (Adam, 2007). Consequently, a 10 m deep soil deposit is deemed sufficient for minimising the boundary effects. There were nearly 190,000 elements in each of the finite element models, and each of the numerical models adopted four different loading phases, including initial equilibrium of soil deposit, application of weight of roller drum, application of cyclic loading simulating roller vibration and equilibrium after removal of the roller and completion of the compaction.

2.4. Roller-soil interface modelling and boundary conditions

Appropriate interfaces are required to simulate the soil-drum interaction capturing stress transfer via interacting surfaces. In this study, 12-node triangular interface elements with 6-point Gaussian integration were utilised to capture any possible soil deflection and drum vibratory displacement while the soil was interacting with the drum (Fig. 5). The behaviour of the interface was evaluated by implementing the linear elastic-perfectly plastic constitutive model (Fatahi et al., 2020). The interface strength reduction factor R_{inter} was adopted via the following equations:

$$c_{\text{i}} = c_{\text{s}} R_{\text{inter}} \tag{13}$$

$$\tan\varphi_{\text{i}} = \tan\varphi_{\text{s}} R_{\text{inter}} \leq \tan\varphi_{\text{s}} \tag{14}$$

$$\sigma_{\text{t,i}} = \sigma_{\text{t,s}} R_{\text{inter}} \tag{15}$$

$$\psi_{\text{i}} = 0^{\circ} \text{ for } R_{\text{inter}} < 1; \text{ otherwise } \psi_{\text{i}} = \psi_{\text{s}} \tag{16}$$

$$G_{\text{i}} = G_{\text{soil}} R_{\text{inter}}^2 \leq G_{\text{soil}} \tag{17}$$

where i and s refer to the interface and soil, respectively; c_{s} and c_{i} are the cohesions of the soil and interface, respectively; σ_{t} is the tensile strength of the soil; φ_{s} and φ_{i} are the friction angles of the soil and interface, respectively; and ψ_{i}, ψ_{s}, G_{i} and G_{soil} are the dilation angles of interface and soil, and shear moduli of interface and soil, respectively. Similar to previous studies (Wehnert and Vermeer, 2004; Aghayarzadeh et al., 2020; Xu et al., 2022), $R_{\text{inter}} = 1$ was adopted, while the zero tension limit was introduced allowing separation of roller drum from the soil surface without any resistance (Brinkgreve et al., 2016).

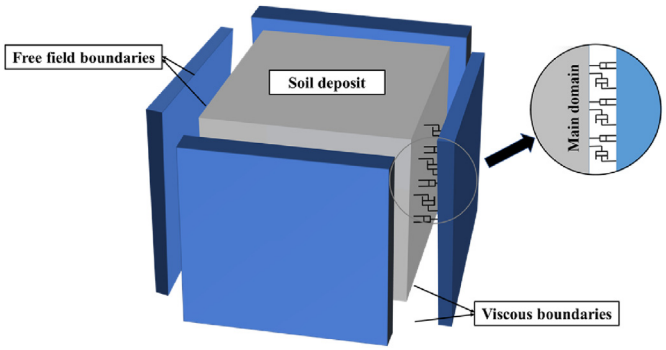

Fig. 6. Adopted numerical model designed for the unbound soil with free-field and viscous boundaries conditions.

Moreover, during the static and dynamic studies, two separate sets of boundary conditions were employed. While considering the gravity loading in the static case, the nodes of the bottom boundary were completely constrained in all directions. In contrast, the lateral displacements on the side boundaries of the model were avoided. Referring to Fig. 6, during the dynamic analysis, while the roller was vibrating, free-field boundaries coupled with independent viscous dashpots were employed to transfer the free-field motion from four side boundaries. Indeed, through the use of resistant tractions in both the tangential and normal directions, the proposed boundary conditions could prevent the wave energy reflecting back into the soil (Fatahi et al., 2020). Moreover, a viscous boundary (non-reflecting boundary condition) with the dampers was used at the bottom boundary during dynamic analysis to absorb the crossing waves without rebounding to reduce wave reflection from the boundaries as suggested by Kenneally et al. (2015) and Herrera et al. (2018) corresponding to the deep soil deposits in situ. The adopted shear and normal tractions on the boundaries to cancel the reflecting waves out were defined as follows (Lysmer and Kuhlemeyer, 1969):

$$t_s = -\rho V_s C_s \tag{18}$$

$$t_n = -\rho V_n C_p \tag{19}$$

where V_s and V_n are the shear and normal components of the velocity, respectively; ρ is the density of the medium; t_s and t_n are the tractions in the shear and normal directions, respectively; and C_s and C_p are the S- and P-wave velocities, respectively. To ensure minimal boundary effects, a block of soil that was 10 m in length, 10 m in width (more than five times larger than the roller length), and 10 m deep (more than six times larger than the roller diameter) was simulated.

3. Development of X-SVR for machine learning

The X-SVR approach adopted for machine learning is briefly introduced to make this paper self-contained. Wang et al. (2020) demonstrated suitability of the X-SVR algorithm to capture the nonlinear relationship among numerous parameters; indeed, the input dataset of X-SVR is mapped into the empirical space by employing the specified kernel function within the nonlinear model, which is also the difference compared with linear X-SVR method (Wang et al., 2020). Furthermore, the X-SVR method can provide information by offering a sampling scheme regarding the statistical moments, cumulative distribution functions and probability density. For readers interested in the detailed derivation of the algorithm, it is recommended to refer to Wang et al. (2020) for an in-depth theoretical description of the X-SVR.

3.1. Linear X-SVR

In typical double-class classification, the selected input $\boldsymbol{x}_{\text{train}} = [\boldsymbol{x}_1, \boldsymbol{x}_2, \boldsymbol{x}_3, ..., \boldsymbol{x}_m]^{\mathrm{T}} \in \Re^{m \times n}$, and the corresponding output $\boldsymbol{y}_{\text{train}} \in \Re^m$, are considered as the training samples, where n represents the corresponding input samples, and m denotes the quality of the selected training dataset. The hyperplane that classifies the classes are denoted by Vapnik (1999) and Drucker et al. (1997):

$$\widehat{f}(\boldsymbol{x}) = \boldsymbol{x}\boldsymbol{w}^{\mathrm{T}} - \delta \tag{20}$$

where $\boldsymbol{w} = [w_1, w_2, w_3, ..., w_n]^{\mathrm{T}} \in \Re^n$ defines the normal to the hyperplane, i.e. the support vector; and $\delta \in \Re$ denotes the bias.

Fig. 7 demonstrates the ε-insensitive band for the support vector regression (SVR) and adopted ε is the tolerance deviation between the prediction $\widehat{f}(\boldsymbol{x})$ and true value $\boldsymbol{y}_{\text{train}}$. The linear regression function Eq. (20) could be alternatively considered as solving the following mathematical programming problem:

$$\min_{\boldsymbol{w},\delta,\xi^*,\xi} : C\sum_{i=1}^{m}(\xi_i^* + \xi_i) + \frac{1}{2}\|\boldsymbol{w}\|_2^2 \tag{21a}$$

$$\text{s.t.} \begin{cases} y_i + \delta - \boldsymbol{x}_i\boldsymbol{w}^{\mathrm{T}} \le \xi_i^* + \varepsilon \\ y_i - \delta + \boldsymbol{x}_i\boldsymbol{w}^{\mathrm{T}} \le \xi_i + \varepsilon \\ \xi_i^*, \xi_i \ge 0 \end{cases} \tag{21b}$$

where $C \in \Re^+ := \{x \in \Re | x > 0\}$ denotes the penalty constant; $\|\cdot\|_2$ denotes the L_2-norm; and ξ_i^* and ξ_i denote the slack variables.

By implementing a similar idea presented in the doubly regularised support vector machine (Dr-SVM) (Wang et al., 2006), both L_1-norm and L_2-norm penalties are applied in combination with the hinge loss function. Moreover, a decomposition process (Dunbar et al., 2010) is utilised to avoid the computation of L_1-norm $\|\boldsymbol{w}\|_1$. A quadratic ε-insensitive loss function (i.e. $l_2^{\varepsilon}(\cdot)$) is also used to enhance the computational stability of the optimisation problems:

$$l_2^{\varepsilon}\left[y_i - \widehat{f}(\boldsymbol{x}_i)\right] = \left| -\widehat{f}(\boldsymbol{x}_i) + y_i \right|^2 \tag{22}$$

As a result, the governing equation for the X-SVR technique is simplified formulated as

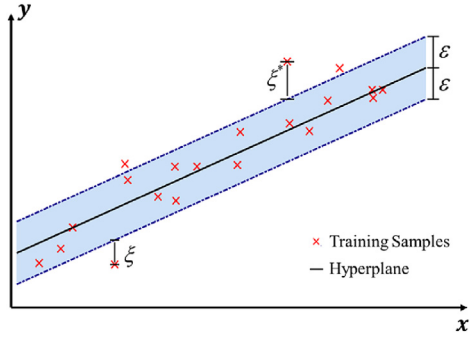

Fig. 7. The ε-insensitive band for a 1D linear SVR.

$$\min_{\widehat{\boldsymbol{z}},\delta}: \ \frac{1}{2}\left(\widehat{\boldsymbol{z}}^{\mathrm{T}}\widehat{\boldsymbol{C}}\widehat{\boldsymbol{z}}+\delta^2\right)+\lambda_2\widehat{\boldsymbol{a}}^{\mathrm{T}}\widehat{\boldsymbol{z}} \tag{23a}$$

$$\text{s.t.}\ \left(\boldsymbol{I}_{(2m+2n)\times(2m+2n)}+\widehat{\boldsymbol{A}}\right)\widehat{\boldsymbol{z}}+\left(\delta\widehat{\boldsymbol{G}}+\varepsilon\boldsymbol{I}_{(2m+2n)\times(2m+2n)}\right)\widehat{\boldsymbol{b}}+\widehat{\boldsymbol{d}}\geq\boldsymbol{0}_{2m+2n} \tag{23b}$$

where $\boldsymbol{I}_{(2m+2n)\times(2m+2n)}\in\Re^{(2m+2n)\times(2m+2n)}$ represents an identity matrix. In addition, to provide the benefits of simultaneously optimising the location and orientation of the regression model, a squared bias parameter (i.e. δ^2) is introduced to the objective function (Mangasarian and Musicant, 2001; Dunbar et al., 2010).

Alternatively, the dual formulation of Eq. (23) could be used to solve as

$$\min_{\varphi}: \ \frac{1}{2}\boldsymbol{\varphi}^{\mathrm{T}}\boldsymbol{Q}\boldsymbol{\varphi}-\boldsymbol{m}^{\mathrm{T}}\boldsymbol{\varphi} \tag{24a}$$

$$\text{s.t.}\ \boldsymbol{\varphi}\geq\boldsymbol{0}_{2m+2n} \tag{24b}$$

where $\boldsymbol{\varphi}\in\Re^{2m+2n}$ represents the Lagrange multiplier vector; and $\boldsymbol{m}\in\Re^{2m+2n}$ and $\boldsymbol{Q}\in\Re^{(2m+2n)\times(2m+2n)}$ are shown in the form of

$$\boldsymbol{m}=\lambda_2\left(\boldsymbol{I}_{(2m+2n)\times(2m+2n)}+\widehat{\boldsymbol{A}}\right)\widehat{\boldsymbol{a}}\widehat{\boldsymbol{C}}^{-1}-\varepsilon\widehat{\boldsymbol{b}}-\widehat{\boldsymbol{d}} \tag{25}$$

$$\boldsymbol{Q}=\widehat{\boldsymbol{C}}^{-1}\left(\widehat{\boldsymbol{A}}+\boldsymbol{I}_{(2m+2n)\times(2m+2n)}\right)\times\left(\boldsymbol{I}_{(2m+2n)\times(2m+2n)}+\widehat{\boldsymbol{A}}\right)^{\mathrm{T}}+\widehat{\boldsymbol{G}}\widehat{\boldsymbol{b}}\widehat{\boldsymbol{b}}^{\mathrm{T}}\widehat{\boldsymbol{G}} \tag{26}$$

Since Eq. (23) is convex, the corresponding dual problem could be effectively solved using any available quadratic programming (QP) solution to achieve the global optimum of the newly X-SVR method, which results in the following linear regression function:

$$\widehat{f}(x)=(\boldsymbol{p}-\boldsymbol{q})^{\mathrm{T}}\boldsymbol{x}-\widehat{\boldsymbol{b}}^{\mathrm{T}}\widehat{\boldsymbol{G}}\boldsymbol{\varphi}^{*} \tag{27}$$

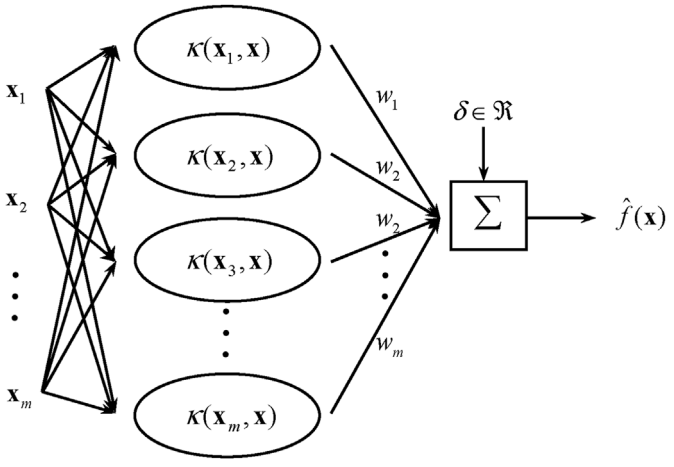

Fig. 8. The framework of the nonlinear X-SVR.

3.2. Nonlinear X-SVR

In additional to the method mentioned above, the nonlinear regression could be fulfilled via an alternative approach known as the empirical kernel map (Scholkopf et al., 1999; Hofmann et al., 2008). The applied empirical kernelisation could be shown as

$$\boldsymbol{x}_i=\left[x_{i,1},x_{i,2},\ldots,x_{i,n}\right]^{\mathrm{T}}\mapsto\widehat{\boldsymbol{\kappa}}(\boldsymbol{x}_i)=\begin{bmatrix}\boldsymbol{\Phi}(\boldsymbol{x}_1)^{\mathrm{T}}\boldsymbol{\Phi}(\boldsymbol{x}_i)\\ \boldsymbol{\Phi}(\boldsymbol{x}_2)^{\mathrm{T}}\boldsymbol{\Phi}(\boldsymbol{x}_i)\\ \vdots\\ \boldsymbol{\Phi}(\boldsymbol{x}_m)^{\mathrm{T}}\boldsymbol{\Phi}(\boldsymbol{x}_i)\end{bmatrix}=\begin{bmatrix}\kappa(\boldsymbol{x}_1,\boldsymbol{x}_i)\\ \kappa(\boldsymbol{x}_2,\boldsymbol{x}_i)\\ \vdots\\ \kappa(\boldsymbol{x}_m,\boldsymbol{x}_i)\end{bmatrix}\quad(i=1,2,\ldots,m) \tag{28}$$

where $\boldsymbol{\Phi}(\boldsymbol{x}_i)$ illustrates the implicit mapping function, which converts the i th input data $\boldsymbol{x}_i\in\Re^n$ into an infinitely dimensional Hilbert feature space or a higher-dimensional Euclidian space; and $\widehat{\kappa}(\boldsymbol{x}_i)$ illustrates the i th component with the empirical degree m of the empirical feature vector (Scholkopf et al., 1999). The empirical feature space is a term given to the m-dimensional vector space (Xiong et al., 2005). In addition, to build the learning model, the empirical feature vector $\widehat{\kappa}(\boldsymbol{x}_i)$ is utilised as the i th training sample. The nonlinear X-SVR framework is described in Fig. 8.

Therefore, for a generalised training dataset $\boldsymbol{x}_{\text{train}}$ and a pre-selected kernel function $\kappa(\cdot,\cdot)$, the initially selected training samples are transformed through the kernel matrix $\boldsymbol{\kappa}_{\text{train}}\in\Re^{m\times m}$, which can be expressed as

$$\boldsymbol{\kappa}_{\text{train}}=\begin{bmatrix}\kappa(\mathbf{x}_1,\mathbf{x}_1) & \kappa(\mathbf{x}_1,\mathbf{x}_2) & \cdots & \kappa(\mathbf{x}_1,\mathbf{x}_m)\\ \kappa(\mathbf{x}_2,\mathbf{x}_1) & \kappa(\mathbf{x}_2,\mathbf{x}_2) & \cdots & \kappa(\mathbf{x}_2,\mathbf{x}_m)\\ \vdots & \vdots & \ddots & \vdots\\ \kappa(\mathbf{x}_m,\mathbf{x}_1) & \kappa(\mathbf{x}_m,\mathbf{x}_2) & \cdots & \kappa(\mathbf{x}_m,\mathbf{x}_m)\end{bmatrix} \tag{29}$$

Furthermore, by employing the kernel matrix $\boldsymbol{\kappa}_{\text{train}}$ as the training dataset, the governing equation of the nonlinear X-SVR could be formulated as

$$\min_{\widehat{\boldsymbol{z}}_\kappa,\delta}: \ \frac{1}{2}\left(\widehat{\boldsymbol{z}}_\kappa^{\mathrm{T}}\widehat{\boldsymbol{C}}_\kappa\widehat{\boldsymbol{z}}_\kappa+\delta^2\right)+\lambda_2\widehat{\boldsymbol{a}}_\kappa^{\mathrm{T}}\widehat{\boldsymbol{z}}_\kappa \tag{30a}$$

$$\text{s.t.}\ \left(\widehat{\boldsymbol{A}}_\kappa+\boldsymbol{I}_{4m\times4m}\right)\widehat{\boldsymbol{z}}_\kappa+\left(\varepsilon\boldsymbol{I}_{4m\times4m}+\delta\widehat{\boldsymbol{G}}_\kappa\right)\widehat{\boldsymbol{b}}_\kappa+\widehat{\boldsymbol{d}}_\kappa\geq\boldsymbol{0}_{4m} \tag{30b}$$

The optimisation program described in Eq. (30) could also be addressed by applying the Lagrange approach to its dual under the Karush-Kuhn-Tucker (KKT) conditions. Consequently, the kernelised X-SVR is expressed as

$$\widehat{f}\ (\boldsymbol{x})=(\boldsymbol{p}_\kappa-\boldsymbol{q}_\kappa)^{\mathrm{T}}\boldsymbol{\kappa}(\boldsymbol{x})-\widehat{\boldsymbol{b}}_\kappa^{\mathrm{T}}\widehat{\boldsymbol{G}}_\kappa\boldsymbol{\varphi}_\kappa^{*} \tag{31}$$

The nonlinear counterpart of the X-SVR preprocesses the input samples by the kernelised function into the empirical space, which is in contrast to the linear X-SVR. Consequently, the convexity of the model is well retained since the X-SVR with the kernel is similar to the linear model with the manipulated input variables (Wang et al., 2019).

The series expansion of the Gegenbauer polynomial (Wu et al., 2006; Yin et al., 2016) is applied to the X-SVR as its kernelised model, and the univariate Gegenbauer polynomials $P_{\widehat{d}}^{\alpha}(x)$ satisfy the recurrence relation:

$$P_0^{\alpha}(x)=1 \tag{32a}$$

$$P_1^{\alpha}(x) = 2\alpha x \tag{32b}$$

$$P_{\widehat{d}}^{\alpha}(x) = \frac{1}{\widehat{d}}\left[2x\left(\widehat{d}+\alpha-1\right)P_{\widehat{d}-1}^{\alpha}(x) - \left(\widehat{d}+2\alpha-2\right)P_{\widehat{d}-2}^{\alpha}(x)\right] \quad \left(\widehat{d}=2,3,4,\ldots\right) \tag{32c}$$

where $\widehat{d}\in\mathbb{Z}_0^+ := \{x\in\mathbb{Z}|x \geq 0\}$ denotes the polynomial sequence, and α denotes the parameter with a positive value. The Gegenbauer weight function $\rho^{\alpha}(x)$ is orthogonal to the Gegenbauer polynomials for a given α over $x\in[-1,1]$, which can be described as

$$\int_{-1}^{1}\rho^{\alpha}(x)P_{\widehat{i}}^{\alpha}(x)P_{\widehat{j}}^{\alpha}(x)\mathrm{d}x = h_{\widehat{i}}^{\alpha}\delta_{\widehat{ij}} \quad \left(\widehat{i},\widehat{j}=0,1,\ldots,\widehat{d}\right) \tag{33}$$

where $\rho^{\alpha}(x)$, $h_{\widehat{i}}^{\alpha}$ and $\delta_{\widehat{ij}}$ can be formulated as

$$\rho^{\alpha}(x) = \left(1-x^2\right)^{\alpha-\frac{1}{2}} \tag{34}$$

$$h_{\widehat{i}}^{\alpha} = \frac{\pi 2^{1-2\alpha}\Gamma\left(\widehat{i}+2\alpha\right)}{\widehat{i}!\left(\widehat{i}+\alpha\right)\Gamma^2(\alpha)} \tag{35}$$

$$\delta_{\widehat{ij}} = \begin{cases} 0 & \left(\widehat{i}\neq\widehat{j}\right) \\ 1 & \left(\widehat{i}=\widehat{j}\right) \end{cases} \tag{36}$$

In Eq. (35), $\Gamma(\cdot)$ denotes the Gamma function. By employing the strategy utilised for characterising the generalised vector inputs of the Chebyshev polynomial (Ye et al., 2006; Ozer et al., 2011; Moghaddam and Hamidzadeh, 2016), the generalised Gegenbauer polynomials can be demonstrated as

$$P_0^{\alpha}(\boldsymbol{x}) = 1 \tag{37a}$$

$$P_1^{\alpha}(\boldsymbol{x}) = 2\alpha\boldsymbol{x} \tag{37b}$$

$$P_{\widehat{d}}^{\alpha}(\boldsymbol{x}) = \frac{1}{\widehat{d}}\left[2\boldsymbol{x}^{\mathrm{T}}\left(\widehat{d}+\alpha-1\right)P_{\widehat{d}-1}^{\alpha}(\boldsymbol{x}) - \left(\widehat{d}+2\alpha-2\right)P_{\widehat{d}-2}^{\alpha}(\boldsymbol{x})\right] \quad \left(\widehat{d}=2,3,4,\ldots\right) \tag{37c}$$

where $\boldsymbol{x}\in\Re^n$ illustrates the column vector of input samples. Gaussian kernel function has a better capacity to capture the local information when compared to the initially applied square root function (Ozer et al., 2011; Cheng et al., 2017), and it is employed as the weighting function for the generalised Gegenbauer kernel (GGK). Therefore, the $\widehat{d}$ th order GGK function $\kappa_{\mathrm{GGK}}{}^{\widehat{d}}(\boldsymbol{x}_i,\boldsymbol{x}_j)$ of two arbitrary input vectors $\boldsymbol{x}_i$ and $\boldsymbol{x}_j$ is shown as

$$\kappa_{\mathrm{GGK}}^{\widehat{d}}(\boldsymbol{x}_i,\boldsymbol{x}_j) = \frac{\sum_{\widehat{k}=0}^{\widehat{d}}P_{\widehat{k}}^{\alpha}(\boldsymbol{x}_i)^{\mathrm{T}}P_{\widehat{k}}^{\alpha}(\boldsymbol{x}_j)}{\exp\left(\left\|\boldsymbol{x}_i-\boldsymbol{x}_j\right\|_2^2\gamma\right)} \tag{38}$$

3.3. Selection of the X-SVR model parameters

The X-SVR with GGK has seven hyperparameters, including two positive kernel scale variables γ and α, the polynomial order $\widehat{d}$, the insensitive tube width ε, the penalty parameter C, and two regularisation parameters λ_1 and λ_2 (Wang et al., 2019).

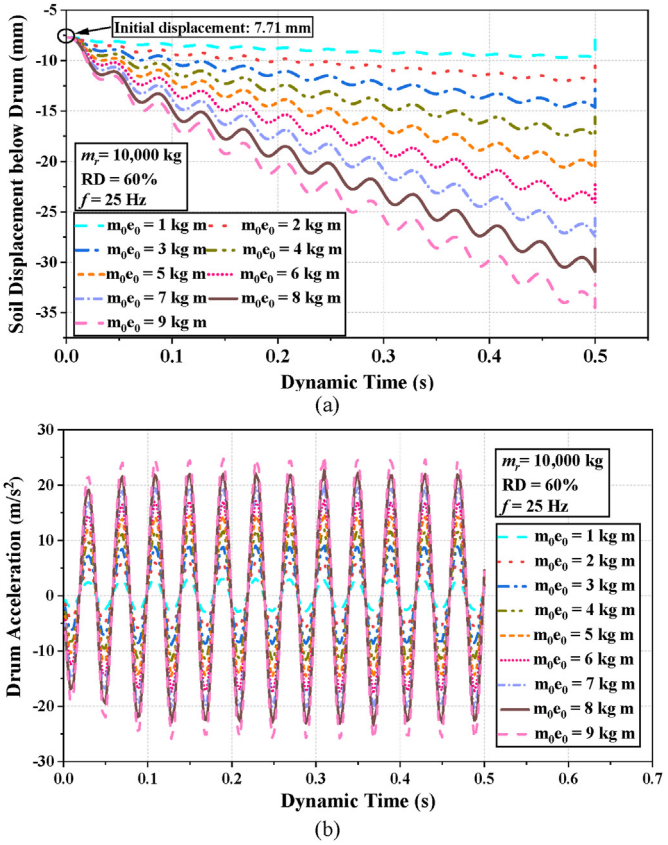

Fig. 9. (a) Soil surface settlement and (b) Drum acceleration response for different eccentric mass moments.

Generally, to assure the generalised capability of the high predicting regression function, the k-fold cross-validation (CV) over the training samples method is employed (Schölkopf et al., 2002). This method is also applied in this regression method to eliminating the overfitting. $Err_{5\mathrm{CV}}$ is the 5-fold CV error, which is applied to representing the measurement of the training error, and it can be shown as

$$Err_{5\mathrm{CV}} = \frac{1}{5}\sum_{\vartheta=1}^{5}err_{\vartheta} \tag{39}$$

where err_{ϑ} is the mean squared error between the prediction value and the true function value. More specifically, we have

$$err_{\vartheta} = \frac{1}{m_{\vartheta}}\sum_{\varpi=1}^{m_{\vartheta}}\left[\boldsymbol{y}_{\vartheta,\varpi}-\widehat{f}_{\vartheta}\left(\boldsymbol{x}_{\vartheta,\varpi}\right)\right]^2 \ (\vartheta=1,2,\ldots,5) \tag{40}$$

where $\boldsymbol{y}_{\vartheta,\varpi}$ is the ϖ th component of $\boldsymbol{y}_{\vartheta}$, m_{ϑ} is the number of training samples in the fold ϑ, $\boldsymbol{x}_{\vartheta}\in\Re^{m_{\vartheta}\times n}$ holds the training samples of the ϑ th fold, $\boldsymbol{x}_{\vartheta,\varpi}\in\Re^n$ represents the ϖ th component of $\boldsymbol{x}_{\vartheta}$, and $\widehat{f}_{\vartheta}(\cdot)$ describes the model prediction in the ϑ th fold. In addition, a nonlinear programming solver named *fmincon* was used in the MATLAB optimisation toolbox as the optimiser engine (Higham and Higham, 2016), and it is utilised to figure out the minimum of a constrained non-linear multivariable function. The logic of the *fmincon* solver employed in this study is shown below:

$$\min_{x} : f(x) \tag{41a}$$

$$\text{s.t.} \begin{cases} \boldsymbol{A} \cdot x \le \boldsymbol{b} \\ \boldsymbol{A}_{\text{eq}} \cdot x = \boldsymbol{b}_{\text{eq}} \\ c(x) \le 0 \\ c_{\text{eq}}(x) = 0 \\ lb \le x \le ub \end{cases} \tag{41b}$$

where $f(x)$, $c(x)$ and $c_{\text{eq}}(x)$ are the nonlinear functions; x_0 is the initial guess; $\boldsymbol{A}_{\text{eq}}$ and $\boldsymbol{A}$ are the matrices, which represent linear equality constraints and linear inequality constraints, respectively; $\boldsymbol{b}_{\text{eq}}$ and $\boldsymbol{b}$ are the vectors which are linear equality constraints and linear inequality constraints, respectively; and ub and lb are a set of upper bound and lower bound on the design variables in x, respectively. It should be noted that x, lb and ub can be scalar or vector. Additionally, it is required to consider three aspects of using *fmincon* function for the optimisation approach: (i) objective function, (ii) constraints, and (iii) the determination of initial values. Appropriate selection of the initial values allows the *fmincon* function to achieve a desired optimal solution.

4. Results and discussion

To better understand the response of roller sitting on the geomaterial subjected to drum vibration, impacts of amplitude, drum frequency, weight of roller and the soil characteristics were investigated. This section also demonstrates the results of the training datasets from the developed inverse solver using a novel kernel-based machine learning technique to determine the soil properties according to the acceleration response of the roller and roller characteristics.

4.1. Effects of vibration amplitude of the drum

Vibratory eccentric force amplitude, a fundamental parameter in the compaction process, directly impacts the compaction quality. Therefore, the eccentric mass moment varying from 1 kg m to 9 kg m was adopted to assess the influences of the excitation force amplitude on the interaction between drum and soil. Fig. 9 shows a predicted example corresponding to different eccentric force amplitudes for the soil relative density of 60% while keeping a constant mass of drum (i.e. 10,000 kg) and a constant frequency (i.e. f = 25 Hz). The compacted soil surface and the vibratory drum kept

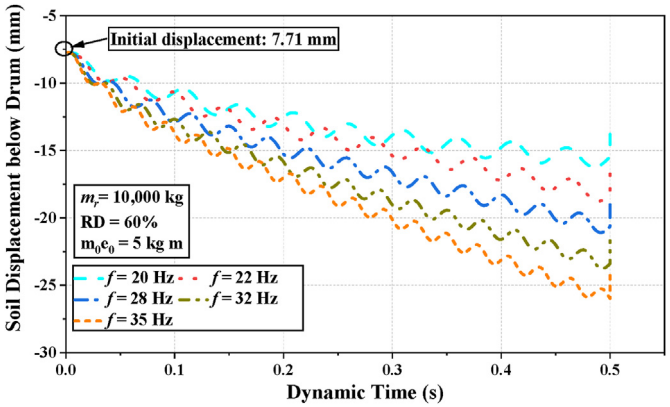

Fig. 10. Soil settlement vs. dynamic time for different vibration frequencies.

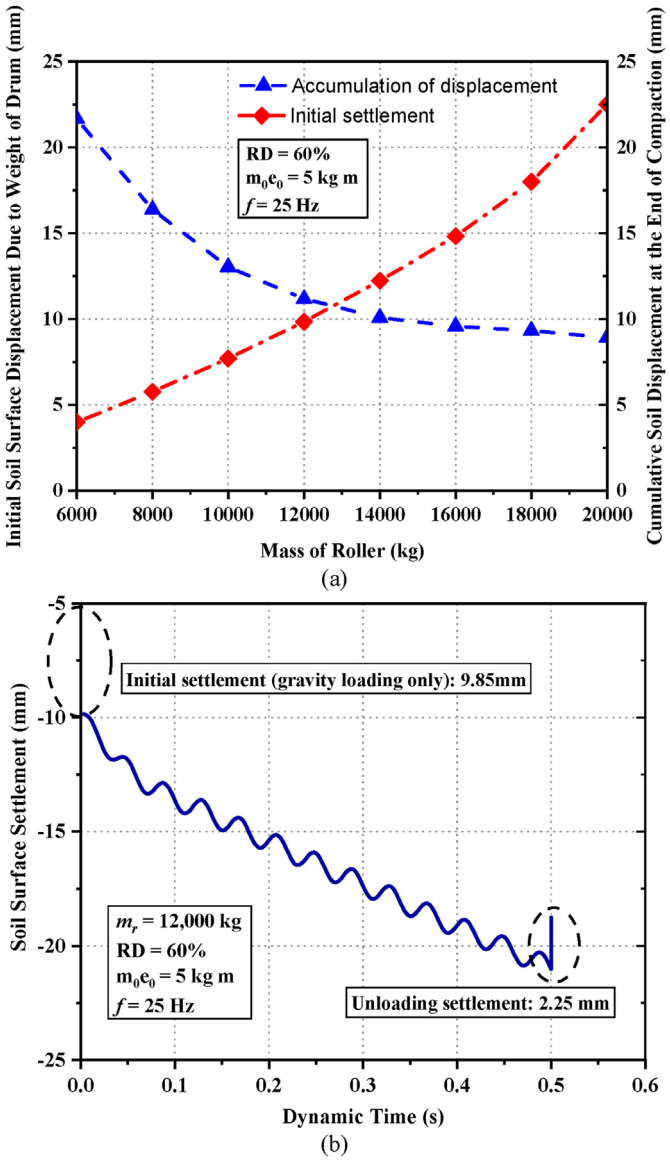

Fig. 11. (a) Initial soil settlement and (b) Time-dependent soil displacement.

continuous contact throughout the entire vibration period. It should be cognizant that a lower eccentric mass moment is frequently used for the finishing passes and proof rolling to prevent over compaction, while a higher eccentric mass moment provides larger excitation force amplitudes at the initial stage of construction to achieve a higher degree of compaction (Kenneally et al., 2015).

Fig. 9a demonstrates the time history of soil surface settlement beneath the drum with various eccentric mass moments. Referring to Fig. 9a, the cumulative soil settlement gradually increased as a result of cyclic loading with the highest settlement observed when m_0e_0 = 9 kg m, and a reduction in geomaterial settlement was observed as a result of a reduction in the eccentric mass moment, similar to observations from other studies (Masad et al., 2016; Ma et al., 2021). Because of the constant weight of the roller and operation frequency, the excitation force was directly influenced by the eccentric mass amplitude, where amplified eccentric mass moment corresponded to the increased acceleration experienced by the drum, as observed in Fig. 9b. Indeed, for the adopted case here, to achieve a higher degree of compaction, a high eccentric mass moment from the vibratory drum could help increase the soil

compression level and vice versa. However, as Kenneally et al. (2015) suggested, high eccentric masses should be avoided in the finishing passes, which would induce irregular drum behaviour caused by bifurcation of the chaotic jump for the densely compacted underlying soil.

4.2. Effects of vibration frequency of the drum

The choice of vibratory roller frequency is crucial for soil compaction (Wersäll et al., 2017). In this study, the operation frequency of the vibratory roller was altered between 20 Hz and 35 Hz. For example, prediction for $RD = 60\%$, corresponding to the unit weight of 17.4 kN/m^3, while the mass of the roller was equal to 10,000 kg and the eccentric mass moment was equal to 5 kg m, is presented in Fig. 10. Referring to Table 3 for the corresponding soil parameters, the average shear wave velocity (S-wave) and compressional wave velocity (P-wave) of the soil deposit at $p^{ref} = 100$ kPa were 238.4 m/s and 389.3 m/s, respectively. The first natural frequency of underlying properties (i.e. $V_p/(4H)$), considering the roller influence depth of 0.6–1 m (Adam, 2007), was estimated to be 97–162 Hz, which is well above the adopted vibration frequency of the drum, and thus no resonance condition was observed.

Fig. 10 presents the surface displacement of the compacted subgrade with dynamic time as a function of changing vibratory roller operation frequency. The results exhibit that an increase in the operation frequency led to increased compacted soil settlement. Numerical predictions show that the highest degree of soil compaction for the adopted sandy soil was achieved when the frequency was equal to 35 Hz, which illustrated that the roller could achieve the optimum compaction when the roller frequency was closer to the first mode natural frequency of the ground, which is consistent with observations made by other researchers (Masad et al., 2016; Wersäll and Larsson, 2016). Referring to the case with a drum vibration frequency of $f = 35$ Hz as in Fig. 10, the initial soil displacement due to roller static gravity load was 7.7 mm, and the maximum vertical displacement reached 25.9 mm at the end of the dynamic phase, and then resumed to 23.98 mm permanent settlement after removing the roller. The compacted soil bounced back 2 mm, which was well less than the initial settlement of 7.7 mm, which clearly shows that the unloading phase comprised only elastic deformation, whereas the initial loading stage subjected to the weight of the roller included both plastic and elastic components.

Fig. 10 explains that the plastic deformation increases due to soil settlement on each dynamic loading cycle as the dynamic duration raises. The irreversible deformation of the selected sandy material reveals that the soil yield stress has gradually increased (Xu et al., 2022). Indeed, the excitation frequency near the natural frequency of compacted soil (i.e. $f = 35$ Hz in this study) resulted in more soil compaction and ground settlement as expected (Pietzsch and Poppy, 1992). Thus, as the vibration frequency reduced (less than the first mode natural frequency of the ground), the cumulative soil displacement decreased, as shown in Fig. 10.

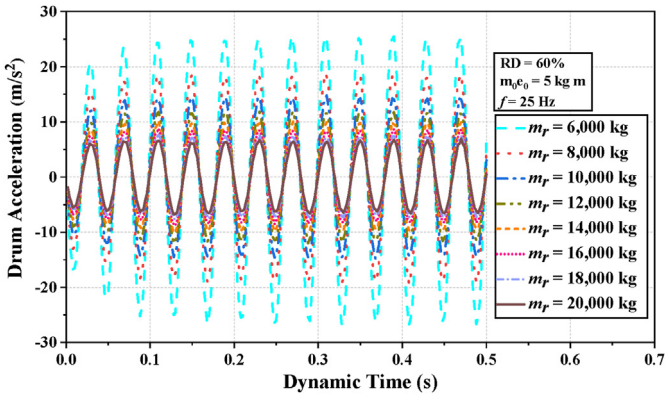

Fig. 12. Drum acceleration vs. dynamic time for different roller masses.

4.3. Effects of roller mass

The mass of the roller (m_r) was incrementally changed from 6000 kg to 20,000 kg to investigate its effects on the drum-soil interaction. As an example of results corresponding to the soil relative density of $RD = 60\%$, the impacts of the mass of the roller are presented in Fig. 11, while the frequency of vibratory roller was equal to 25 Hz and the eccentric mass moment was $m_0e_0 = 5$ kg m. Fig. 11a illustrates the impacts of the roller mass on the initial soil displacement because of the weight of the roller and cumulative soil displacement after 10 cycles of loading. Moreover, Fig. 11b demonstrates the accumulated soil settlement varying with dynamic time for the 12,000 kg roller, which obviously examines how the cumulative plastic deformations in the soil gradually increased.

The initial settlement due to gravity loading alone for the heavier roller (i.e. 20,000 kg roller, 22.5 mm initial settlement) was more than the initial settlement for the lighter roller (i.e. 6000 kg roller, 4 mm initial settlement) because of the enhanced static pressure implemented to the compacted soil. For the 12,000 kg roller with operation eccentric mass moment $m_0e_0 = 5$ kg m (Fig. 11b), the unloading soil displacement (i.e. 2.25 mm) due to the roller removal was smaller than the initial displacement (i.e. 9.85 mm) induced by the self-weight of the roller, highlighting that the initial settlement included both plastic and elastic components. Referring to Fig. 12, the lightest 6000 kg roller had the highest acceleration responses and caused the highest values of the cumulative soil displacement after the completion of roller compaction. The predictions indicate that with increasing roller acceleration, the total settlement of compacted soil increased, and it is consistent with the observations made by Cao et al. (2010). For a given centrifugal force, the added weight of the roller lowered the roller acceleration and vibratory compaction.

4.4. Evaluation of the machine learning method

To illustrate the feasibility of using machine learning to back calculate the soil stiffness based on the drum acceleration response, the comprehensive results from the 3D numerical modelling were used. The newly proposed generalised Gegenbauer, a series expansion of the Gegenbauer polynomial (Stein and Weiss, 2016), was implemented herein as the kernel for the X-SVR method to train and test the experimental data. In this study, there were 1405 sets of data from the 3D numerical method, which were used to examine the ability of machine learning to determine compacted soil stiffness. Among them, 405 sets of data (around 30% of the total datasets) were randomly selected to train the network, and 1000 sets of data (around 70% of the total datasets) were used to test the trained network. It should be noted that several research studies utilised a large portion of data for testing and evaluation. For example, the selection of 30% training data and 70% testing data was employed by Lin et al. (2017) for target classification through a convolutional highway unit which is a novel architecture developed based on the convolutional neural network (CNN), and the classification accuracy of the model could reach 94.47%. In addition, experimental data by Zainudin et al. (2016) were split into different distributions of training and testing data under different machine learning classification techniques. They showed that the data group

of 30% training and 70% testing had the best results for predictions under the decision tree and random forest (RF) classification techniques, and the data group of 20% training and 80% testing had the best precisions for classification techniques of Naïve Bayes and support vector machine.

The influence depth of compacted soil is primarily contingent upon the operating parameters, dimensions, as well as weight of the roller (Fathi et al., 2021a). Adjusting various independent operating settings of the employed rollers by the driver, such as frequency and eccentric mass moment, can directly impact the progress in compaction and quality of compaction (Pietzsch and Poppy, 1992). In addition, the acceleration response of the roller is closely related to compaction level, impacting the soil stiffness (Hua et al., 2018). Indeed, to assess the real-time stiffness extraction of the proposed numerical model based on the vibration response of the roller drum, the four physical parameters were selected as the machine learning inputs, including: (1) the acceleration vs. dynamic time of drum ($\ddot{z}_d$ or a_d), (2) frequency of dynamic loading (f), (3) ratio of eccentric mass to drum length ($R_{el} = m_0 e_0 / l$) and (4) ratio of roller mass to drum length ($R_{ml} = M/l$), while the unloading/reloading modulus (E_{ur}) was selected as the output. It should be noted that these input parameters can be directly collected from the roller during compaction. Thus, in real practice, engineers can use the developed machine learning technique to determine equivalent properties of the soil below the roller within the influence depth of the roller. Additionally, roller operation parameters (f, R_{el} and R_{ml}) are independent and can be decided or controlled by the manufacturer or operator, and drum acceleration response ($\ddot{z}_d - t_d$) is influenced by the compacted soil characteristics. These input parameters can be directly collected from the roller without requiring further data from the soil. Moreover, to cover a wide range of vibratory roller characteristics, the applied excitation frequencies varied from 20 Hz to 35 Hz, with roller mass ranging from 5000 kg to 20,000 kg and the excitation force induced by the eccentric mass moment was set from 1 kg m to 9 kg m. Furthermore, to confirm the accuracy of the established machine learning method, the root mean square error (*RMSE*), coefficient of determination (R^2) and relative error (*RE*) were calculated from the following equations:

$$RMSE = \sqrt{\frac{1}{s}\sum_{i=1}^{s}(y_i - \hat{y}_i)^2} \tag{42}$$

$$R^2 = 1 - \frac{\sum_i(-y_i + \hat{y}_i)^2}{\sum_i(-\bar{y} + \hat{y}_i)^2} \tag{43}$$

$$RE = \frac{\hat{y} - y}{y} \times 100\% \tag{44}$$

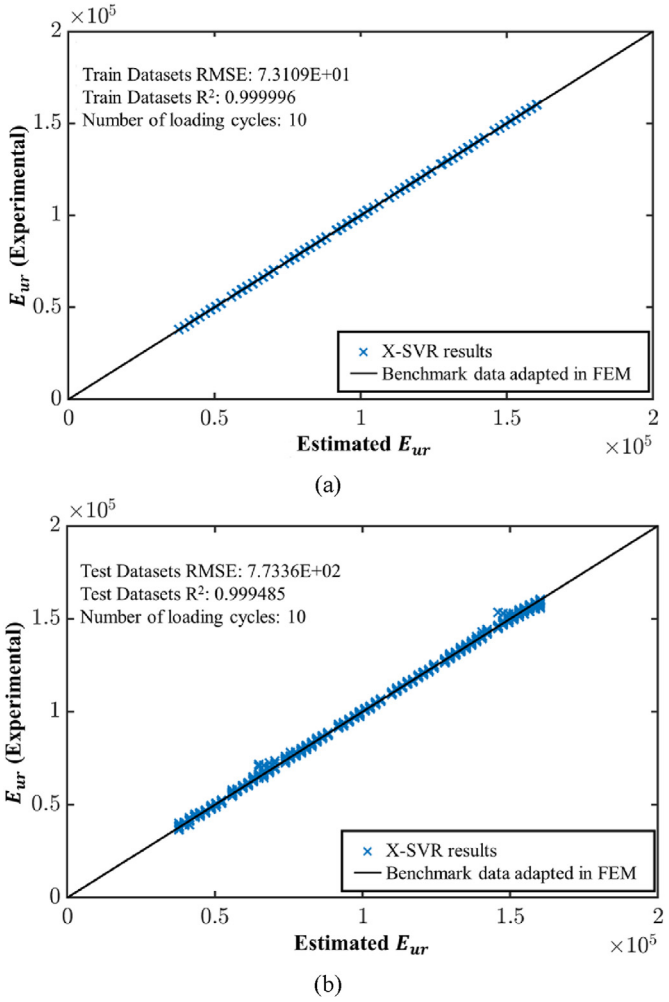

Fig. 13. Comparison of finite element results (experiment) with machine learning outputs (estimated) for (a) training data and (b) testing data.

where y, $\hat{y}$ and $\bar{y}$ denote the values of benchmark, prediction and the mean of the true values, respectively; while s denotes the number of samples.

To assess the accuracy of the machine learning technique for real-time feedback control, the adopted machine learning function should result in a high coefficient of determination on training and testing experimental data. The root means square error (*RMSE*), coefficient of determination (R^2) and relative error (*RE*) for the cases using different kernels, including the Gegenbauer kernel, linear kernel, polynomial kernel, Gaussian kernel and exponential kernel, are presented in Table 4. The training and testing unloading/reloading moduli (E_{ur}) exhibited the best correlation with the

Table 4
Comparisons of the performance of adopted machine learning techniques with different kernel functions.

Kernel function	$RMSE_{train}$	R^2_{train}	RE_{train} (%)	$RMSE_{test}$	R^2_{test}	RE_{test} (%)
Gegenbauer	7.3109×10^1	0.999996	0.00044	7.7336×10^2	0.999485	0.5115
Linear	6.0993×10^3	0.968795	0.26537	7.9158×10^3	0.9487	0.61204
Polynomial	6.2967×10^3	0.966725	0.28918	7.9367×10^3	0.947896	0.55768
Gaussian	7.2005×10^2	0.999568	0.01186	1.1838×10^3	0.998782	0.16686
Exponential	1.0801×10^2	0.999973	0.00262	2.4892×10^3	0.994455	0.30239

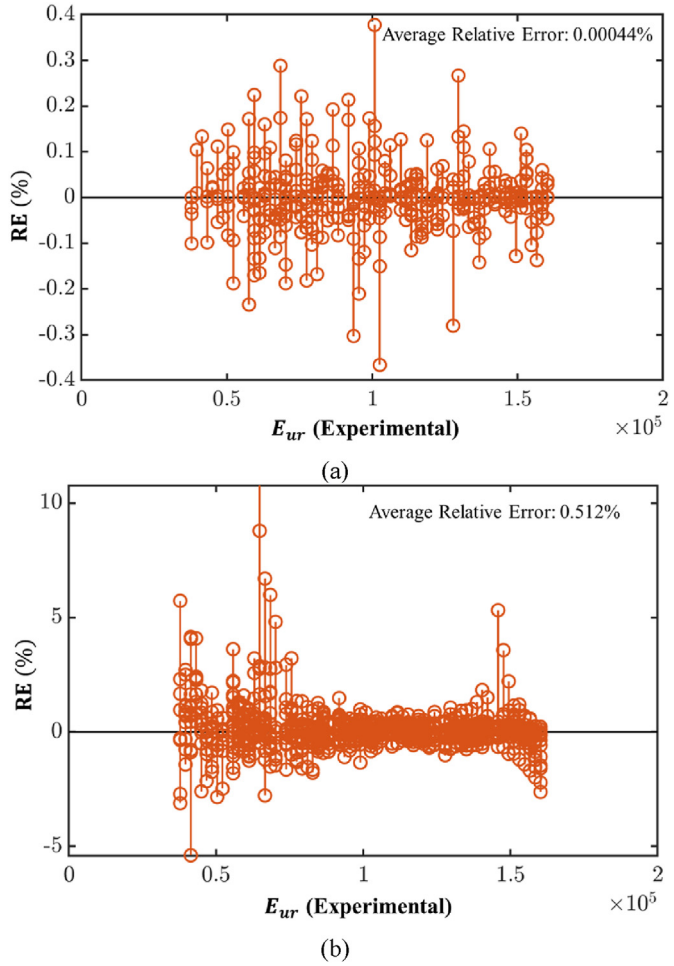

Fig. 14. The relative errors of the machine learning predictions adopting Gegenbauer kernel for (a) training data and (b) testing data.

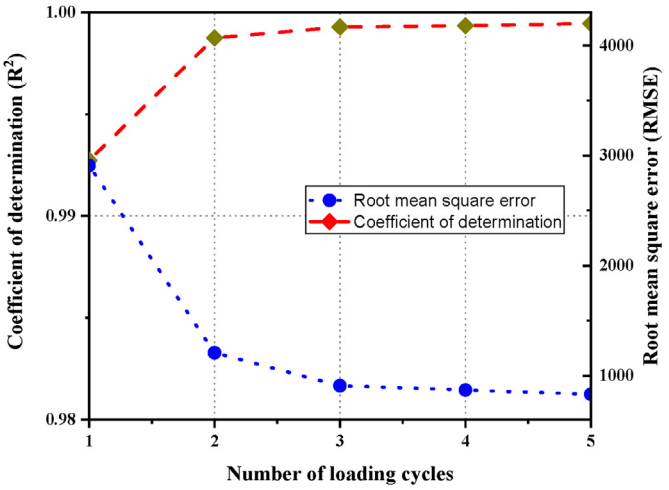

Fig. 15. Coefficient of determination and root mean square error of machine learning method with Gegenbauer kernel vs. number of loading cycles.

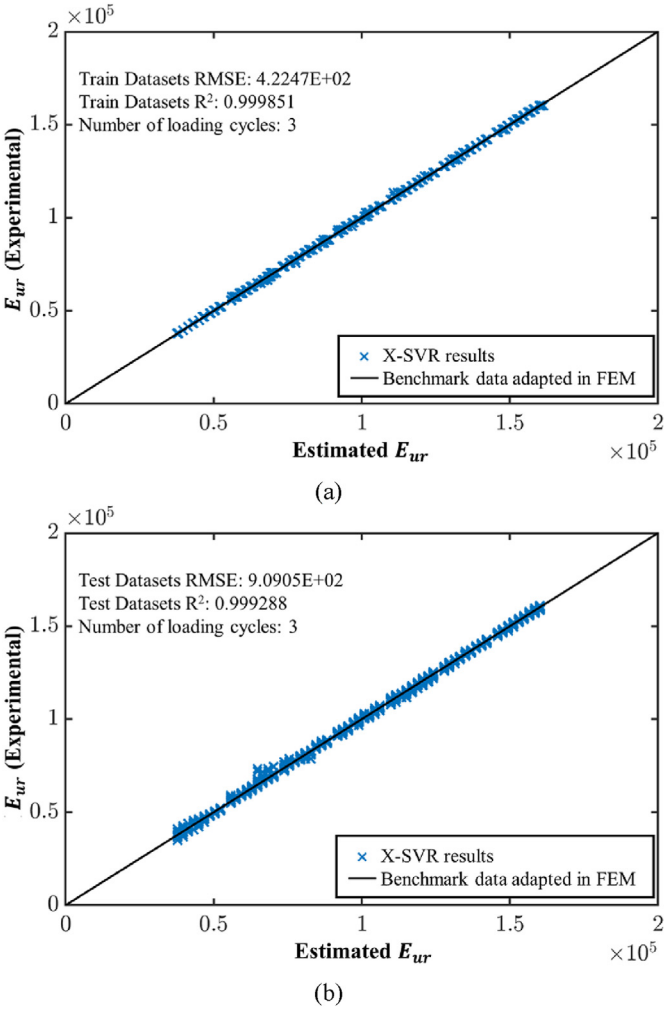

Fig. 16. Comparison of finite element results (experiment) with machine learning outputs (estimated) on three loading cycles for (a) training data and (b) testing data.

experimental data with the Gegenbauer kernel and the coefficient of determination for training and testing data with the Gegenbauer kernel were 0.999996 and 0.999485, respectively (Fig. 13a). In addition, the relative error of the adopted machine learning method with the Gegenbauer kernel function exhibited the lowest value, which is also reported in Fig. 14. The average relative errors of the adopted machine learning process with the Gegenbauer kernel method for training and testing data were less than 0.00044% and 0.512%, respectively, indicating the adopted model had high precision for both training and testing data. The average computation time of each numerical modelling case using selected parameters for the X-SVR algorithm with the Gegenbauer kernel function was 0.2 s (Local workstation with 8 Intel Core i7-6700 - 3.4 GHz cores – 32 GB RAM – 1 TB hard-drive), which makes the machine learning technique suitable for real-time quality control by practising engineers on site.

The proposed X-SVR method in this study can be theoretically formulated as a QP problem, which can efficiently capture the global optimum because of its strong convexity related to the QP problem. Furthermore, the developed scheme has been integrated with advanced kernels (e.g. GGK in this study) and an optimisation toolbox to improve the efficiency and robustness of solving engineering problems (Wang et al., 2020). In comparison to the conventional SVR method, X-SVR can establish a higher-accuracy regression model between the inputs and outputs by utilising identical sizes of training datasets. This study applied the ANN model for comparing its performances with the adopted X-SVR. The accuracy of the predictive capacity (R^2) of the ANN approach for

training and testing experimental data were 0.996423 and 0.953048, respectively, and the adopted X-SVR with GGK function represented the better training and testing unloading/reloading moduli with 0.999996 and 0.999485, respectively. In addition, the average relative errors of the adopted model in the study for training and testing data were less than 0.00044% and 0.512%, respectively, which is better than ANN for training and testing data, which were 0.04072% and 0.53%, respectively. While this study has clearly highlighted the great potential of machine learning in IC, further studies to assess the potential use of other machine learning algorithms, such as the multi-layer perceptron (MLP) feed-forward neural network model (Fathi et al., 2021b), machine learning support vector machine algorithm (Zhang et al., 2021) and RF and ANN hybrid machine learning algorithm (Fathi et al., 2019) are also recommended.

4.5. Effects of the number of loading cycles on predictions using machine learning

Evaluating the minimum required time duration to collect drum acceleration data as input for machine learning training and predictions of the unloading/reloading modulus (E_{ur}) in real-time depends on the vibration frequency of the drum. The results of each loading cycle were analysed thoroughly, and Fig. 15 summarises the accuracy of predictions considering the number of loading cycles used for developing a machine learning inverse solver. Referring to Fig. 15, the coefficient of determination gradually increased due to the increased number of loading cycles used for back calculation, and after three loading cycles, minor changes in R^2 and *RMSE* were observed. According to the implemented machine learning analyses, the results indicated that applying X-SVR with GGK when the number of utilised loading cycles was equal to or larger than three was reasonable.

Fig. 16 shows the comparison of estimated and experimental unloading/reloading moduli (E_{ur}) when three loading cycles were used in the machine learning process for training data and testing data, confirming acceptable coefficient of determination R^2. Therefore, the minimum field time interval needed to use for real-time determination of E_{ur} using the X-SVR method with the Gegenbauer kernel can be calculated by

$$T_i = N_c \frac{1}{f} \tag{45}$$

where T_i and N_c denote the minimum input working period for satisfactory machine learning precision and the minimum number of loading cycles (determined to be $N_c = 3$ as in Fig. 16), respectively. This study can be used as preliminary research for properly choosing training data and efficiently back-calculating the soil unloading/reloading modulus in real time during the compaction process. Thus, the proposed machine learning technique can be used as feedback control, which can be used as potential guidance by practising engineers for determining the soil unloading/reloading modulus to be used for quality assurance.

In this study, total stress analysis was used, and the back-calculated soil stiffness is for the entire soil matrix representing the equivalent value as it is in situ and in the total stress domain. Soil water content impacts the soil stiffness characteristics and the response of the roller. It is recommended that more rigorous soil constitutive models for unsaturated soils should be adopted for future research studies; for example, advanced constitutive models such as the extended Barcelona model (BBMx) (Pedroso and Farias, 2011), Barcelona basic model (BBM) (Alonso et al., 1990) and SFG model (Sheng et al., 2008) can be the options to be explored in future research studies. Moreover, Ng et al. (2020) adopted a modified HS-Small model by incorporating suction effects on soil, and such an option can also be considered. Furthermore, since a single layer soil was adopted in the finite element modelling in this study, the results can be used as a preliminary evaluation of the equivalent soil parameters below the roller. Further studies are required to obtain the individual soil layer stiffness values for multi-layer soil profiles.

5. Conclusions

IC technology has emerged to provide uniform and high-quality compaction with real-time feedback. As an integrated mechanism, the magnitudes of roller parameters can be initiatively optimised to achieve the most efficient compaction effort. Many of the existing models employed simplified soil models as well as discrete dynamic analysis, while they cannot model hysteretic damping, stiffness degradation, cyclic loading and dissipative properties of the geomaterials. Since the continuum nature of the geomaterials cannot be explicitly described by mass-elastic spring-linear dashpot system often used in the literature, accurately back calculation of the real soil parameters during the compaction process remains a great challenge for practising engineers.

This paper presented details of a 3D numerical model to simulate the interaction between the vibratory roller drum and the soil beneath to be used for real-time back calculation of the soil stiffness. The effects of the amplitude, frequency and the weight of roller were assessed numerically and used to develop a comprehensive database for machine learning. The database was used to train the inverse solver using a newly proposed kernel-based X-SVR approach to predict the unloading/reloading modulus of underlying geomaterial according to the acceleration response of the drum during compaction.

In this study, to numerically estimate the dynamic behaviour of the soil-drum system, numerical modelling via PLAXIS 3D was adopted. Indeed, more than a thousand 3D dynamic analyses were implemented to assess the influences of different drum parameters on the drum response and soil deformations during compaction. The modified model adopted a typical drum size based on the practice in Australia, which was 2.1 m in length and 1.5 m in diameter, sitting on uniform soil. The adopted HS-Small constitutive soil model was able to evaluate the nonlinear stress-strain response of the soil subjected to cyclic loading, particularly variations of damping and soil stiffness with shear strain. The characteristics of compacted soil used in the numerical modelling were very diverse, covering a wide range from loose to dense states of granular soils, corresponding to relative densities of 20%–90%.

The FEM predictions showed that the eccentric force amplitude greatly impacted the soil surface settlement right below the drum. Indeed, an eccentric mass m_0 rotating along the axle of the drum with an effective moment arm e_0 induced the centrifugal force corresponding to m_0e_0 altering between 1 kg m and 9 kg m in this study. When the constant weight of the roller and operation frequency was applied, the excitation force was directly influenced by the eccentric mass amplitude. Therefore, a higher degree of compaction could be achieved by adopting a high eccentric mass moment. Considering the importance of the frequency of roller vibration in the compaction process, this study also investigated the effects of operation frequency in the common range of 20–35 Hz. The simulated results showed that the vibratory compaction could result in more compaction effort when the roller frequency was closer to the natural frequency of the soil.

The newly proposed kernel-based X-SVR method integrated with the IC system was proposed in this paper for real-time extraction of underlying soil modulus during compaction. The proposed method could predict the soil stiffness based on the X-

SVR algorithm with the Gegenbauer kernel using the acceleration response of the drum and basic roller properties. Both training and testing unloading/reloading moduli (E_{ur}) obtained from the machine learning method correlated well with the 3D finite element predictions considering the nonlinear elastoplastic soil model and dynamic soil-drum interaction. It is evident that the inverse solver developed in this study could predict the soil stiffness utilising the novel kernel-based X-SVR machine learning accurately and in the reasonably short time required for real-time quality control by practising engineers.

Declaration of competing interest

The authors declare that they have no known competing financial interests or personal relationships that could have appeared to influence the work reported in this paper.

List of symbols

C	Penalty constant
C_p	P-wave velocity
C_s	S-wave velocity
c	Soil cohesion
c_i	Cohesion of interface
c_f	Suspension damping (MN s/m)
c_s	Cohesion of soil
$\widehat{d}$	Order of the polynomial
e_0	Arm of the rotating mass
err_ϑ	Mean squared error
E_{50}	Primary deviatoric loading (kPa)
E_{50}^{ref}	Secant stiffness when $p^{ref} = 100$ kPa
E_D	Dissipated energy
E_{oed}	Tangent stiffness (kPa)
E_{oed}^{ref}	Tangent stiffness when $p^{ref} = 100$ kPa
E_S	Cyclic maximum strain energy in a single load cycle
E_{ur}	Unloading and reloading stress-dependent stiffness from the drained triaxial test (kPa)
E_{ur}^{ref}	Unloading/reloading stiffness related to the reference pressure ($p^{ref} = 100$ kPa)
F_c	Drum-soil system contact force (kN)
F_{ecc}	Centrifugal force (kN)
f	Frequency of vibratory drum
G_0	Small-strain shear stiffness
G_0^{ref}	Shear modulus at the reference pressure ($p^{ref} = 100$ kPa)
G_i	Shear modulus of interface
G_s	Secant shear stiffness
G_{soil}	Shear modulus of soil
G_t	Small strain tangent shear modulus
G_{ur}	Unloading/reloading shear modulus
$\boldsymbol{I}$	Identity matrix
g	Gravitational acceleration (9.81 m/s^2)
K_0^{nc}	Stress ratio in primary compression
$\widehat{\boldsymbol{\kappa}}(\boldsymbol{x}_i)$	The ith training sample for constructing the learning model
k_f	Suspension stiffness (MN/m)
l	Length of the drum
M	Mass of the roller
m	Power for the stress-level dependency of the soil stiffness
m_0	Equipment rotating mass (kg)
m_d	Drum mass (kg)
m_f	Frame mass (kg)
m_r	Roller mass (kg)
N_c	Minimum number of loading cycles
p^{ref}	Reference pressure ($p^{ref} = 100$ kPa)
q	Deviatoric stress
q_a	Asymptotic value of the shear strength
R^2	Coefficient of determination
R_{el}	Ratio of eccentric mass to drum length
R_f	Failure ratio
R_{inter}	Interface strength reduction factor
R_{ml}	Ratio of roller mass to drum length
s	Number of samples
T_i	Minimum input working period for superior machine learning precision
t	Time (s)
t_n	Tractions in the normal direction
t_s	Tractions in the shear direction
V_n	Normal component of velocity
V_s	Shear component of velocity
$\boldsymbol{w}$	Support vector
$\boldsymbol{x}$	Column vector of input variables
y	Values of benchmark
$\widehat{y}$	Prediction
$\bar{y}$	Mean of the true values
z_d	Displacement of drum
$\dot{z}_d$	Velocity of drum
$\ddot{z}_d$	Acceleration of drum
z_f	Displacement of frame
$\dot{z}_f$	Velocity of frame
$\ddot{z}_f$	Acceleration of frame
α	Constant value ($\alpha = 0.385$)
$\Gamma(\cdot)$	Gamma function
$\gamma_{0.7}$	Shear strain when G_s is reduced to 0.7 G_0
γ_c	Shear strain
δ	Bias
ε_1	Vertical strain
ξ	Hysteretic damping ratio
ξ_i	Allowable negative deviation
ξ_i^*	Positive excessive deviation
ρ	Density of medium
σ_3	Minor principal stress
σ_t	Tensile strength
$\boldsymbol{\Phi}(\boldsymbol{x}_i)$	Implicit mapping function
$\boldsymbol{\varphi}$	Lagrange multiplier vector
φ	Friction angle
φ_s	Friction angle of soil
φ_i	Friction angle of interface
ψ_s	Dilation angle of soil
ψ_i	Dilation angle of interface
ω	Angular frequency (Hz)
$\|\cdot\|_2$	L_2-norm

References

Adam, D., 2007. Roller integrated continuous compaction control (CCC) technical contractual provisions & recommendations. In: Correia, A.G., Momoya, Y., Tatsuoka, F. (Eds.), Design and Construction of Pavements and Rail Tracks: Geotechnical Aspects and Processed Materials. Taylor & Francis Group, London, UK, pp. 111–138.

Adam, D., Pistrol, J., 2016. Dynamic roller compaction for earthworks and roller-integrated continuous compaction control: state of the art overview and recent developments. In: Proceedings of the Conferenze di Geotecnica di Torino, XXIV Ciclio. Italy, Turin, pp. 1–41.

Aghayarzadeh, M., Khabbaz, H., Fatahi, B., Terzaghi, S., 2020. Interpretation of dynamic pile load testing for open-ended tubular piles using finite-element method. Int. J. GeoMech. 20 (2), 04019169.

Alonso, E.E., Gens, A., Josa, A., 1990. A constitutive model for partially saturated soils. Geotechnique 40 (3), 405–430.

Alzabeebee, S., 2021. Influence of soil model complexity on the seismic response of shallow foundations. Geomech. Eng. 24 (2), 193–203.

An, Z., Liu, T., Zhang, Z., Zhang, Q., Huangfu, Z., Li, Q., 2020. Dynamic optimization of compaction process for rockfill materials. Autom. ConStruct. 110, 103038.

Anderegg, R., Kaufmann, K., 2004. Intelligent compaction with vibratory rollers: feedback control systems in automatic compaction and compaction control. Transport. Res. Rec. 1868 (1), 124–134.

Asif Imran, S., Barman, M., Commuri, S., Zaman, M., Nazari, M., 2018. Artificial neural network-based intelligent compaction analyzer for real-time estimation of subgrade quality. Int. J. GeoMech. 18 (6), 04018048.
Beainy, F., Commuri, S., Zaman, M., 2014. Dynamical response of vibratory rollers during the compaction of asphalt pavements. J. Eng. Mech. 140 (7), 04014039.
Benz, T., 2007. Small-strain Stiffness of Soils and its Numerical Consequences. PhD Thesis. Universitat of Stuttgart. Germany, Stuttgart.
Benz, T., Schwab, R., Vermeer, P., 2009. Small-strain stiffness in geotechnical analyses. Bautechnik 86, 16–27.
Bhandari, S., Khabbaz, H., Fatahi, B., Lee, J., Xu, Z., Zhong, J., 2022. Evaluating the influence of soil plasticity on the vibratory roller-soil interaction for intelligent compaction. In: Tutumluer, E., Nazarian, S., Al-Qadi, I., Qamhia, I.I.A. (Eds.), Advances in Transportation Geotechnics IV. Springer, pp. 247–260.
Brinkgreve, R., Engin, E., Engin, H.K., 2010. Validation of empirical formulas to derive model parameters for sands. In: Benz, T., Nordal, S. (Eds.), Numerical Methods in Geotechnical Engineering. CRC Press, Hong Kong, China.
Brinkgreve, R., Kappert, M., Bonnier, P., 2007. Hysteretic Damping in a Small-strain Stiffness Model. In: Proceedings of the Numerical Models in Geomechanics (NUMOG X), Rhodes. Greece, pp. 737–742.
Brinkgreve, R., Kumarswamy, S., Swolfs, W., Waterman, D., Chesaru, A., Bonnier, P., 2016. PLAXIS 2016. PLAXIS bv, Netherlands.
Buechler, S.R., Mustoe, G.G., Berger, J.R., Mooney, M.A., 2012. Understanding the soil contact problem for the LWD and static drum roller by using the DEM. J. Eng. Mech. 138 (1), 124–132.
Burland, J., 1989. Ninth Laurits Bjerrum Memorial Lecture: “Small is beautiful”—the stiffness of soils at small strains. Can. Geotech. J. 26 (4), 499–516.
Cao, L., Zhou, J., Li, T., Chen, F., Dong, Z., 2021. Influence of roller-related factors on compaction meter value and its prediction utilizing artificial neural network. Construct. Build. Mater. 268, 121078.
Cao, Y.-W., Liang, N.-X., Qin, M., Lu, Z.-F., 2010. Research on the correlation between vibration acceleration of roller and compaction degree of subgrade soil. In: Proceedings of the ASCE 10th International Conference of Chinese Transportation Professionals. USA, Reston, VA, pp. 2974–2982.
Chang, G., Xu, Q., Rutledge, J., et al., 2011. Accelerated implementation of intelligent compaction technology for embankment subgrade soils, aggregate base, and asphalt pavement materials. In: Technical Report No. FHWA-IF-12-002. Federal Highway Administration, Washington, D.C., USA.
Cheng, K., Lu, Z., Wei, Y., Shi, Y., Zhou, Y., 2017. Mixed kernel function support vector regression for global sensitivity analysis. Mech. Syst. Signal Process. 96, 201–214.
Dos Santos, J., Correia, A., 2001. Reference threshold shear strain of soil. Its application to obtain an unique strain-dependent shear modulus curve for soil. In: Proceedings of the 15th International Conference on Soil Mechanics and Geotechnical Engineering. Turkey, Istanbul, pp. 267–270.
Drucker, H., Burges, C.J., Kaufman, L., Smola, A., Vapnik, V., 1997. Support Vector Regression Machines. in: Proceedings of the Advances in Neural Information Processing Systems 9, pp. 155–161. Cambridge, MA, USA.
Dunbar, M., Murray, J.M., Cysique, L.A., Brew, B.J., Jeyakumar, V., 2010. Simultaneous classification and feature selection via convex quadratic programming with application to HIV-associated neurocognitive disorder assessment. Eur. J. Oper. Res. 206 (2), 470–478.
Erdmann, P., Adam, D., 2014. Numerical simulation of dynamic soil compaction with vibratory compaction equipment. In: Brandl, H., Adam, D. (Eds.), Proceedings of the XV Danube-European Conference on Geotechnical Engineering. Austria, Vienna, pp. 243–248.
Fatahi, B., Huang, B., Yeganeh, N., Terzaghi, S., Banerjee, S., 2020. Three-dimensional simulation of seismic slope–foundation–structure interaction for buildings near shallow slopes. Int. J. GeoMech. 20 (1), 04019140.
Fathi, A., 2020. Extracting Mechanical Properties of Compacted Geomaterials Using Intelligent Compaction Technology. The University of Texas at El Paso, Texas, USA. PhD Thesis.
Fathi, A., Mazari, M., Saghafi, M., Hosseini, A., Kumar, S., 2019. Parametric study of pavement deterioration using machine learning algorithms. In: Proceedings of the Airfield and Highway Pavements 2019: Innovation and Sustainability in Highway and Airfield Pavement Technology. American Society of Civil Engineers, Reston, VA, USA, pp. 31–41.
Fathi, A., Tirado, C., Rocha, S., Mazari, M., Nazarian, S., 2021a. Assessing depth of influence of intelligent compaction rollers by integrating laboratory testing and field measurements. Transp. Geotech. 28, 100509.
Fathi, A., Tirado, C., Rocha, S., Mazari, M., Nazarian, S., 2021b. A machine-learning approach for extracting modulus of compacted unbound aggregate base and subgrade materials using intelligent compaction technology. Infrastructure 6 (10), 142.
FHWA, 2017. Intelligent Compaction Measurement Values (ICMV). Department of Transportation, Washington, D.C., USA.
Forssblad, L., 1980. Compaction meter on vibrating rollers for improved compaction control. In: Proceedings of the International Conference on Compaction. France, Paris, pp. 541–546.
Han, B., Zdravkovic, L., Kontoe, S., Taborda, D.M., 2016. Numerical investigation of the response of the Yele rockfill dam during the 2008 Wenchuan earthquake. Soil Dyn. Earthq. Eng. Times 88, 124–142.
Hardin, B.O., Drnevich, V.P., 1972. Shear modulus and damping in soils: design equations and curves. J. Soil Mech. Found Div. 98 (7), 667–692.
Herrera, C., Costa, P.A., Caicedo, B., 2018. Numerical modelling and inverse analysis of continuous compaction control. Transp. Geotech. 17, 165–177.
Higham, D.J., Higham, N.J., 2016. MATLAB Guide. SIAM.
Hofmann, T., Schölkopf, B., Smola, A.J., 2008. Kernel methods in machine learning. Ann. Stat. 36 (3), 1171–1220.
Hu, W., Polaczyk, P., Gong, H., Ma, Y., Huang, B., 2021. Visualization and quantification of soil laboratory impact compaction. J. Rock Mech. Geotech. Eng. 14 (2), 616–624.
Hua, T., Yang, X., Yao, Q., Li, H., 2018. Assessment of real-time compaction quality test indexes for rockfill material based on roller vibratory acceleration analysis. Adv. Mater. Sci. Eng. 2018, 2879321.
Kawa, M., Puła, W., Truty, A., 2021. Probabilistic analysis of the diaphragm wall using the hardening soil-small (HSs) model. Eng. Struct. 232, 111869.
Kenneally, B., Musimbi, O.M., Wang, J., Mooney, M.A., 2015. Finite element analysis of vibratory roller response on layered soil systems. Comput. Geotech. 67, 73–82.
Kontoe, S., Zdravkovic, L., Potts, D., Menkiti, C., 2011. On the relative merits of simple and advanced constitutive models in dynamic analysis of tunnels. Geotechnique 61 (10), 815–829.
Krober, W., Floss, E.R., Wallrath, W., 2001. Dynamic soil stiffness as quality criterion for soil compaction. In: Proceedings of the Geotechnics for Roads, Rail Tracks and Earth Structures. A.A. Balkema, Rotterdam, Netherlands, pp. 189–199.
Kuwano, R., 2018. Advanced Laboratory Stress-Strain Testing of Geomaterials, 1st ed. Routledge, England, UK.
Lavin, P., 2003. Asphalt Pavements: A Practical Guide to Design, Production and Maintenance for Engineers and Architects. CRC Press, Spon, London.
Lin, Z., Ji, K., Kang, M., Leng, X., Zou, H., 2017. Deep convolutional highway unit network for SAR target classification with limited labeled training data. IEEE Geosci. Remote. Sens. Lett. 14 (7), 1091–1095.
Liu, H., Zou, D., Liu, J., 2014. Constitutive modeling of dense gravelly soils subjected to cyclic loading. Int. J. Numer. Anal. Methods GeoMech. 38 (14), 1503–1518.
Lundberg, V.G., 1939. Elastische beruehrung zweier halbraeume. Forsch. Ing. Wes 10 (5), 201–211.
Lysmer, J., Kuhlemeyer, R.L., 1969. Finite dynamic model for infinite media. J. Eng. Mech. Div. 95 (4), 859–877.
Ma, Y., Wang, Z., Zhang, Y., 2021. Research on numerical simulation of intelligent compaction of subgrade secondary development based on ABAQUS finite element. J. Civ. Eng. 9 (12), 1424–1437.
Mangasarian, O.L., Musicant, D.R., 2001. Lagrangian support vector machines. J. Mach. Learn. Res. 1 (3), 161–177.
Masad, E., Scarpas, A., Rajagopal, K.R., Kassem, E., Koneru, S., Kasbergen, C., 2016. Finite element modelling of field compaction of hot mix asphalt. Part II: Applications. Int. J. Pavement Eng 17 (1), 24–38.
Moghaddam, V.H., Hamidzadeh, J., 2016. New Hermite orthogonal polynomial kernel and combined kernels in support vector machine classifier. Pattern Recogn. 60, 921–935.
Mooney, M.A., 2010. Intelligent soil compaction systems. In: Final Report, NCHRP 676. Transportation Research Board, Washington, D.C., USA.
Mooney, M.A., Facas, N.W., 2013. Extraction of layer properties from intelligent compaction data. In: Technical Report NCHRP 145. Transportation Research Board, Washington, D.C., USA.
Mooney, M.A., Rinehart, R.V., 2007. Field monitoring of roller vibration during compaction of subgrade soil. J. Geotech. Geoenviron. Eng. 133 (3), 257–265.
Mooney, M.A., Rinehart, R.V., 2009. In situ soil response to vibratory loading and its relationship to roller-measured soil stiffness. J. Geotech. Geoenviron. Eng. 135 (8), 1022–1031.
Nazarian, S., Fathi, A., Tirado, C., Kreinovich, V., Rocha, S., Mazari, M., 2020. Evaluating mechanical properties of earth material during intelligent compaction. In: Technical Report NCHRP 933. University of Texas at El Paso.
Ng, C.W.W., Zheng, G., Ni, J., Zhou, C., 2020. Use of unsaturated small-strain soil stiffness to the design of wall deflection and ground movement adjacent to deep excavation. Comput. Geotech. 119, 103375.
Ozer, S., Chen, C.H., Cirpan, H.A., 2011. A set of new Chebyshev kernel functions for support vector machine pattern classification. Pattern. Recognit. 44 (7), 1435–1447.
Pedroso, D.M., Farias, M.M., 2011. Extended Barcelona basic model for unsaturated soils under cyclic loadings. Comput. Geotech. 38 (5), 731–740.
Pei, T., Yang, X., 2018. Compaction-induced stress in geosynthetic-reinforced granular base course–A discrete element model. J. Rock Mech. Geotech. Eng. Times 10 (4), 669–677.
Pietzsch, D., Poppy, W., 1992. Simulation of soil compaction with vibratory rollers. J. Terramechanics 29 (6), 585–597.
Ranasinghe, R., Jaksa, M., Kuo, Y., Nejad, F.P., 2017. Application of artificial neural networks for predicting the impact of rolling dynamic compaction using dynamic cone penetrometer test results. J. Rock Mech. Geotech. Eng. 9 (2), 340–349.
Saberi, M., Annan, C.-D., Konrad, J.-M., 2020. Three-dimensional constitutive model for cyclic behavior of soil-structure interfaces. Soil Dyn. Earthq. Eng. Times 134, 106162.
Schanz, T., Vermeer, P., Bonnier, P.G., 2019. The hardening soil model: formulation and verification. In: Proceedings of the beyond 2000 in Computational Geotechnics. Routledge, Amsterdam, Netherlands, pp. 281–296.
Scholkopf, B., Mika, S., Burges, C.J., et al., 1999. Input space versus feature space in kernel-based methods. IEEE Trans. Neural Network. 10 (5), 1000–1017.
Schölkopf, B., Smola, A.J., Bach, F., 2002. Learning with Kernels: Support Vector Machines, Regularization, Optimization, and beyond. MIT Press, Cambridge, MA, USA.

Scott, B.T., Jaksa, M.B., Mitchell, P.W., 2020. Influence of towing speed on effectiveness of rolling dynamic compaction. J. Rock Mech. Geotech. Eng. 12 (1), 126–134.
Sharma, V., Kumar, A., 2018. Behavior of ring footing resting on reinforced sand subjected to eccentric-inclined loading. J. Rock Mech. Geotech. Eng. 10 (2), 347–357.
Sheng, D., Fredlund, D.G., Gens, A., 2008. A new modelling approach for unsaturated soils using independent stress variables. Can. Geotech. J. 45 (4), 511–534.
Stein, E.M., Weiss, G., 2016. Introduction to Fourier Analysis on Euclidean Spaces (PMS-32), vol. 32. Princeton University Press.
Van Susante, P.J., Mooney, M.A., 2008. Capturing nonlinear vibratory roller compactor behavior through lumped parameter modeling. J. Eng. Mech. 134 (8), 684–693.
Vapnik, V., 1999. The Nature of Statistical Learning Theory. Springer.
Wang, L., Zhu, J., Zou, H., 2006. The doubly regularized support vector machine. Stat. Sin. 589–615.
Wang, Q., Li, Q., Wu, D., Yu, Y., Tin-Loi, F., Ma, J., Gao, W., 2020. Machine learning aided static structural reliability analysis for functionally graded frame structures. Appl. Math. Model. 78, 792–815.
Wang, Q., Wu, D., Tin-Loi, F., Gao, W., 2019. Machine learning aided stochastic structural free vibration analysis for functionally graded bar-type structures. Thin-Walled Struct. 144, 106315.
Wehnert, M., Vermeer, P., 2004. Numerical analyses of load tests on bored piles. In: Proceedings of the Numerical Methods in Geomechanics. Canada, Ottawa, ON, pp. 505–511.
Wersäll, C., Larsson, S., 2016. Influence of force ratio and frequency on vibratory surface compaction. In: Proceedings of the 3rd International Conference on Geotechnics for Sustainable Infrastructure Development. Vietnam, Hanoi.
Wersäll, C., Nordfelt, I., Larsson, S., 2017. Soil compaction by vibratory roller with variable frequency. Geotechnique 67 (3), 272–278.
Wu, C.-L., Ma, X.-P., Fang, T., 2006. A complementary note on Gegenbauer polynomial approximation for random response problem of stochastic structure. Probabilistic Eng. Mech 21 (4), 410–419.
Wu, W., 1990. The behaviour of very loose sand in the triaxial compression test: discussion. Can. Geotech. J. 27 (1), 159–162.
Xiong, H., Swamy, M., Ahmad, M.O., 2005. Optimizing the kernel in the empirical feature space. IEEE Trans. Neural Network. 16 (2), 460–474.
Xu, Q., Chang, G.K., Gallivan, V.L., 2012. Development of a systematic method for intelligent compaction data analysis and management. Construct. Build. Mater. 37, 470–480.
Xu, Z., Khabbaz, H., Fatahi, B., Lee, J., Bhandari, S., 2022. Numerical assessment of impacts of vibrating roller characteristics on acceleration response of drum used for intelligent compaction. In: Tutumluer, E., Nazarian, S., Al-Qadi, I., Qamhia, I.I.A. (Eds.), Advances in Transportation Geotechnics IV. Springer, pp. 231–245.
Ye, N., Sun, R., Liu, Y., Cao, L., 2006. Support vector machine with orthogonal Chebyshev kernel. In: Proceedings of the 18th International Conference on Pattern Recognition. IEEE, Hong Kong, China, pp. 752–755.
Yin, S., Yu, D., Yin, H., Xia, B., 2016. Interval and random analysis for structure–acoustic systems with large uncertain-but-bounded parameters. Comput. Methods Appl. Mech. Eng. 305, 910–935.
Zainudin, S., Jasim, D.S., Bakar, A.A., 2016. Comparative analysis of data mining techniques for Malaysian rainfall prediction. Int. J. Adv. Sci. Eng. Inf. Technol. 6 (6), 1148–1153.
Zhang, F., Kimura, M., 2002. Numerical prediction of the dynamic behaviors of an RC group-pile foundation. Soils Found. 42 (3), 77–92.
Zhang, W., Khan, A.R., Yoon, S., Lee, J., Zhang, R., Zeng, K., 2021. Investigation of the correlations between the field pavement in-place density and the intelligent compaction measure value (ICMV) of asphalt layers. Construct. Build. Mater. 292, 123439.

Dr. Behzad Fatahi is an award-winning engineer and internationally recognised academic for his work in the field of soil-structure interaction. He has been working at the frontier of new infrastructure and building technologies and solutions, in particular, systems that will make infrastructure (e.g. roads, railways, pipelines, large energy storage tanks) and buildings safer and more resilient. He is currently Head of Discipline (Geotechnical and Transport Engineering) and an Associate Professor of Civil Engineering in the School of Civil and Environmental Engineering at the University of Technology Sydney (UTS) in Australia. Dr. Fatahi has been involved in many ground improvement projects in Australia and overseas. Behzad is a Chartered Professional Engineer (Civil, Geotechnical and Structural Engineering Colleges) and Fellow of Engineers Australia. He was named Australasia Young Railway Engineer of the Year by Engineers Australia and the Railway Technical Society of Australasia. Behzad was also awarded with the first prize at the Young Geotechnical Professional Night, which is a prestigious geotechnical engineering award from the Australian Geomechanics Society. He has supervised 17 PhD candidates to completion as the principal supervisor and has published more than 200 peer-reviewed technical papers in top journals and conference proceedings in the fields of Civil, Geotechnical and Structural Engineering.